Small peptides modulate the immune function of the ion channel-like protein ACD6 in *Arabidopsis thaliana*

Wangsheng Zhu[1,2*], Lei Li[1], Benjamin Neuhäuser[3], Michael Thelen[1,6], Mingyu Wang[2], Junbin Chen[2], Luyang Wei[2], Kavita Venkataramani[1,7], Moises Exposito-Alonso[1,8], Chang Liu[4,5], Jakob Keck[1], A. Cristina Barragan[1], Rebecca Schwab[1], Ulrich Lutz[1], Uwe Ludewig[3], and Detlef Weigel[1*]

[1]Department of Molecular Biology, Max Planck Institute for Developmental Biology, 72076 Tübingen, Germany

[2]China Key Laboratory of Pest Monitoring and Green Management, MOA, and College of Plant Protection, China Agricultural University, 100193, Beijing, China

[3]Nutritional Crop Physiology, University of Hohenheim, 70599 Stuttgart, Germany

[4]Center for Plant Molecular Biology (ZMBP), University of Tübingen, 72076 Tübingen, Germany

[5]Institute of Biology, University of Hohenheim, 70599 Stuttgart, Germany

Current addresses:

[6]Institute for Physical and Theoretical Chemistry, University Tübingen, 72076 Tübingen, Germany

[7]Department of Biology, University of Massachusetts Boston, Boston, MA 02125, USA

[8]Department of Plant Biology, Carnegie Institution for Science, Stanford, CA 94305, USA

[*]Correspondence: zhuws.hzau@gmail.com (W.Z.); weigel@weigelworld.org (D.W.)

Abstract

The quantitative resistance gene *ACCELERATED CELL DEATH 6* (*ACD6*), which encodes a transmembrane protein with intracellular ankyrin repeats, has been implicated in a trade-off between growth and defense among wild strains of *Arabidopsis thaliana*. Naturally hyperactive alleles of the *ACD6*-Est-1 type can lead to spontaneous activation of immune responses, although the extent of visible hyperimmunity in strains with this allele varies substantially. We have identified a natural suppressor locus, *MODULATOR OF HYPERACTIVE ACD6 1* (*MHA1*), which codes for a small protein of ~7 kDa that attenuates activity of the *ACD6*-Est-1 allele. *MHA1* and its paralog *MHA1-LIKE* (*MHAL*) differentially interact with specific *ACD6* variants, and both MHA1 and MHAL peptides can bind to the ACD6 ankyrin repeats. MHAL also enhances accumulation of an ACD6 complex, thereby increasing activity of the *ACD6* standard allele. The ACD6 ankyrin repeats are similar to those of transient receptor potential (TRP) ion channels, and several lines of evidence support that increased ACD6 activity is linked to enhanced calcium signaling. Our work highlights how the study of natural variation reveals new aspects of plant immunity.

Introduction

While plants need to defend themselves against pathogens, an inherent danger is inappropriate activation of immune responses, which can cause collateral damage to the plant itself. Particularly effective immune alleles enable a plant to respond rapidly to pathogen attack, but such variants might also be potentially deleterious. The study of natural variation in the immune system of *Arabidopsis thaliana* has identified *ACCELERATED CELL DEATH 6* (*ACD6*) as a nexus for a trade-off between growth and disease resistance in wild populations (Świadek et al., 2016; Todesco et al., 2014, 2010). ACD6 is a positive regulator of cell death and defense responses and the EMS-induced *acd6*-1 gain-of-function allele has constitutively elevated defenses and a prominent lesion-mimic phenotype (Lu et al., 2003). Similar to *acd6*-1, the naturally hyperactive *ACD6*-Est-1 allele can protect plants against a wide range of unrelated pathogens, but at the same time often exacts a substantial growth penalty in form of reduced stature and leaf necrosis (Todesco et al., 2010). The same is true for the natural hybrid necrosis alleles *ACD6*-Mir-0 and *ACD6*-Se-0 (Todesco et al., 2014).

The hyperimmunity conditioned by increased *ACD6* activity is dependent on salicylic acid (SA), with inactivation of individual SA signaling components, such as *NON-EXPRESSOR OF PR1* (*NPR1*), *ENHANCED DISEASE SUSCEPTIBILITY 1* (*EDS1*) and *PHYTOALEXIN DEFICIENT 4* (*PAD4*), partially suppressing the effects of *ACD6* hyperactivity (Ng et al., 2011; Rate et al., 1999). SA signaling is required for several aspects of plant immunity, including pattern- and effector-triggered immunity (PTI and ETI) as well as systemic acquired resistance (SAR) (Fu and Dong, 2013; Lu et al., 2016; Seyfferth and Tsuda, 2014; Vlot et al., 2009). Both SA biosynthesis and many aspects of SA up- and downstream signaling are well understood, with feedback and feedforward regulation being important mechanisms. A complex of EDS1 and PAD4 functions downstream of nucleotide binding site/leucine rich repeat receptors (NLRs) with an N-terminal Toll/interleukin-1 receptor/resistance protein (TIR) domain to activate SA biosynthesis, and the accumulating SA further enhances EDS1 and PAD4 expression. Similarly, *ACD6* stimulates SA accumulation, and SA in turn enhances

ACD6 mRNA expression and affects the subcellular localization of ACD6 protein (Lu et al., 2003; Zhang et al., 2014). A working model for ACD6 is that it is a redundant key regulator of SA signaling through a positive SA-dependent feedback loop (Lu et al., 2003; Tateda et al., 2014; Zhang et al., 2014). While its exact relationship to PTI, ETI and SAR is not entirely clear, it interacts genetically with an allele of the TIR-NLR gene *SUPPRESSOR OF NPR1-1, CONSTITUTIVE 1* (*SNC1*) (Zhu et al., 2018).

ACD6 encodes a multipass transmembrane protein with nine intracellular ankyrin repeats (Lu et al., 2003; Zhang et al., 2014). ACD6 protein has been found in association with multiple plasma membrane localized pattern recognition receptors (PRRs) and the PRR co-receptor BRI1-ASSOCIATED RECEPTOR KINASE 1 (BAK1), as well as other receptor like kinases, supporting a direct role for ACD6 in plant immunity (Tateda et al., 2014; Zhang et al., 2017, 2014). In response to SA signalling, ACD6 oligomers accumulate at the plasma membrane, indicating that plasma membrane localisation of ACD6 is important for its function (Tateda et al., 2014; Zhang et al., 2014). Another ankyrin-repeat transmembrane protein, BDA1, also functions as a positive regulator of immunity in *A. thaliana* (Yang et al., 2012), and a maize *ACD6* homolog has recently been implicated in smut resistance (Zhang et al., 2019). However, the precise biochemical mechanism by which ACD6 and related proteins act remains enigmatic.

An important theme in plant immunity is that many immune system components can interact in a non-additive manner (Kover and Caicedo, 2001). Epistatic interactions are common in the regulatory and structural gene networks underlying the biosynthesis of plant metabolites, including many metabolites important for defense against pathogens (Soltis and Kliebenstein, 2015). In NLR-mediated disease resistance, different alleles and orthologs of the powdery mildew resistance NLR gene *Pm3* in cereals can interfere with each other's activity (Hurni et al., 2014; Stirnweis et al., 2014). Conversely, there are highly redundant NLR networks of protein-protein interactions in several species (Wróblewski et al., 2018; Wu et al., 2017), and inappropriate interaction among NLRs or between NLRs and other proteins can lead to adverse outcomes in the form of autoimmunity (Li et al., 2020; Tran et al., 2017).

That not all *ACD6*-Est-1 carriers express autoimmunity suggests, however, that the detrimental effects of *ACD6*-Est-1 are often mitigated by second-site modifiers (Todesco et al., 2010; Zhu et al., 2018). Here, from the epistatic interaction of *ACD6* with natural alleles present at an unlinked locus, we identify a new gene family encoding small peptides, MODIFIER OF HYPERACTIVE ACD6 1 (MHA1) and its paralog MHA-LIKE (MHAL), which modulate the activity of ACD6 in a complex manner. Consistent with sequence similarity of ankyrin repeats in ACD6 with those of transient receptor protein (TRP) ion channels from animals and fungi, we find that increased ACD6 activity enhances calcium signaling, either by modulating activity of other ion channels or by ACD6 acting itself as ion channel. Since MHA1 and MHAL both bind to the ankyrin repeats of ACD6 and affect ACD6 activity, we propose that MHA1 and MHAL are ACD6 ligands.

Results

Identification of *MODIFIER OF HYPERACTIVE ACD6 (MHA)* loci

We have previously reported that many, but not all *A. thaliana* accessions carrying the *ACD6*-Est-1 allele express leaf necrosis in the absence of pathogen challenge (Todesco et al., 2010). In several cases, genetic mapping showed that this is due to second site modifiers, with different accessions containing different modifiers (Zhu et al., 2018). Because appreciable population frequency might indicate that an allele has been favored by selection, we were particularly interested in modifiers that are shared by a larger number of accessions. We reasoned that it should be possible to detect such common loci by genome-wide association (GWA) analysis of necrosis severity among accessions with the *ACD6*-Est-1 allele. We first identified such a set through a combination of Sanger sequencing and perusal of short-read data from the 1001 Genomes Project (1001 Genomes Consortium, 2016; Zhu et al., 2018), and scored necrosis on an arbitrary scale in 84 accessions **(Table 1)**. Using the EMMAX algorithm (Grimm et al., 2016), we identified two unlinked regions with significant associations, *MODIFIER OF HYPERACTIVE ACD6 1* (*MHA1*) (Chr1: 22,935,037, $p=10^{-12}$), and *MHA2* (Chr4: 11,019,243, $p=10^{-8}$) **(Figure 1A)**, which together explained over 60% of phenotypic variation.

The most highly associated SNP at *MHA2* is in an intron of *SBT2.2*/AT4G20430 **(Figure 1–figure supplement 1A)**, predicted to encode an extracellular subtilisin-like protease, possibly involved in the regulation of cell death (Ramírez et al., 2013; Schaller et al., 2018). The top SNP at *MHA1* causes a non-synonymous substitution in AT1G62045, which encodes a small protein without domains of known function **(Figure 1–figure supplement 1B)**. At both loci, attenuated *ACD6*-Est-1 dependent necrosis was associated with the minor alleles, found in 17 and 29 accessions, respectively **(Figure 1B)**.

The frequencies of the *MHA1* and *MHA2* alleles were similar in the 87 *ACD6*-Est-1 accessions (of which 84 had been used for GWA) and in the 797 accessions with other *ACD6* alleles from the 1001 Genomes project (1001 Genomes Consortium, 2016). However, we observed that among the *ACD6*-Est-1 GWA accesions, accessions with the *MHA2*-Ty-0 allele were about twice as likely to have the *MHA1*-Ty-0 allele (12/19) than accessions with the standard *MHA2* allele (17/65) **(Figure 1–figure supplement 2A)**. Accordingly, the average linkage disequilibrium between the causal SNP from *MHA1* (Chr1: 22935037) and SNPs across the entire *MHA2* locus was much higher in the *ACD6*-Est-1 population used for GWA than in the non-*ACD6*-Est-1 set of accessions ($p<0.0001$, Wilcoxon nonparametric test) **(Figure 1–figure supplement 2B)**. Haplotype analysis further revealed that the only allele combination that was enriched in the two populations with and without the *ACD6*-Est-1 allele was the combination of both Ty-0-type suppressor alleles at *MHA1* and *MHA2* in accessions with the *ACD6*-Est-1 allele ($p=0.006$, binomial test) **(Figure 1–figure supplement 2C)**. These results suggest that greater suppression of *ACD6*-Est-1 effects is favorable in natural populations.

To confirm linkage of the GWA hits to suppression of *ACD6*-Est-1 induced necrosis, we made use of the accession Ty-0, which has minor alleles at both *MHA1* and *MHA2* **(Figure 1C)**. There were no nonsynonymous differences in *ACD6* between Ty-0 and Est-1 **(Table 2)**, and *ACD6* was well expressed,

although not quite as highly as in Est-1 **(Figure 1D)**. Ty-0 had much less salicylic acid (SA) than Est-1, and reduced expression of the SA-responsive marker gene *PATHOGENESIS-RELATED 1* (*PR1*) **(Figure 1D, E)**. As expected, *ACD6*-Ty-0 and *ACD6*-Est-1 similarly triggered necrotic lesions and reduced biomass when introduced as transgenes into the Col-0 background **(Figure 1F, G)**. Together, these results demonstrate that Ty-0 harbors extragenic suppressors that mask the effects of *ACD6*-Est-1.

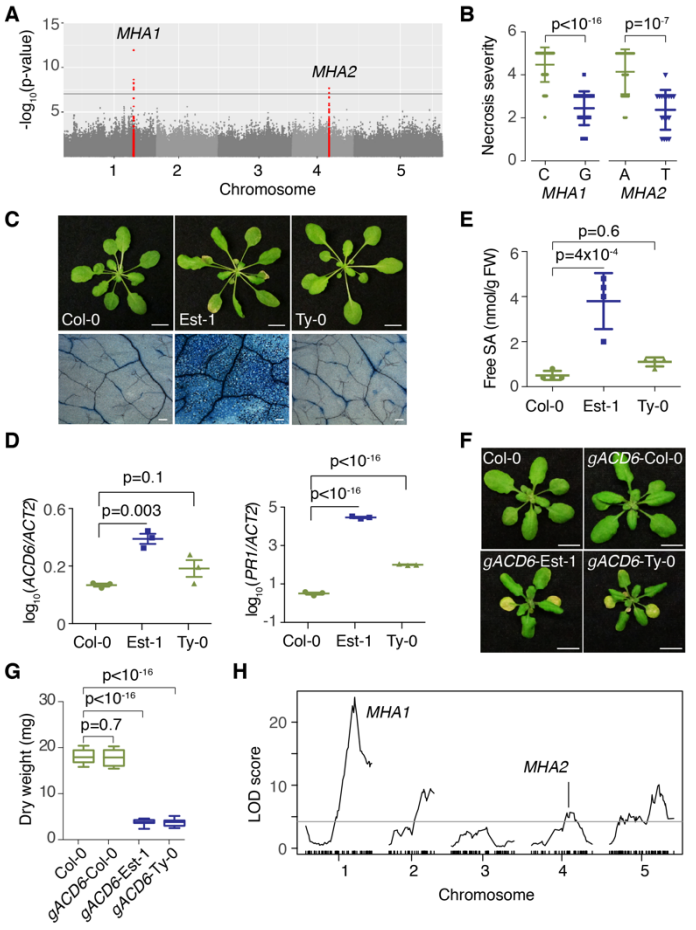

Figure 1. Genetic background dependence of *ACD6*-Est-1 effects. (A) Manhattan plot of GWA scores for necrosis. SNPs within 60 kb of the top SNPs in red. The horizontal gray line indicates a nominal p=0.05 threshold after Bonferroni correction. **(B)** Necrosis score of accessions with different *MHA1* and *MHA2* alleles. **(C)** Top, four-week-old plants with different *ACD6* alleles. Bottom, Trypan Blue-stained sixth leaves. Scale bars, 1 cm (top), 0.2 mm (bottom). **(D)** *ACD6* and *PR1* expression, as measured by RT-qPCR from three biological replicates each. **(E)** Accumulation of free salicylic acid (SA) in different genotypes. **(F)** Eighteen-day old transgenic lines in Col-0 background in 23°C LD. Scale bar, 1 cm. **(G)** Dry weight of 3-week-old plants. **(H)** QTL map of necrosis in Ty-0 x Est-1 F_2 population. Black line, significance threshold of p=0.05 from 1,000 permutations. p-values (B, D, E, G) from Tukey's HSD test.

Since the *ACD6* alleles of Ty-0 and Est-1 had similar activity, a Ty-0 x Est-1 F_2 population provided a straightforward tool for direct mapping of genomic regions associated with suppression of *ACD6*-Est-1 induced necrosis. Linkage analysis identified four QTL in this cross, with none of the QTL including *ACD6* itself, as expected **(Figure 1H, Figure 1–figure supplement 3A, B)**. The GWA hit *MHA2* was included in the confidence interval of a QTL on chromosome 4 that explained 9% of phenotypic variation. Overexpression of the major allele of *SBT2.2* triggered *ACD6*-dependent spotted cell death in the Col-0 background at 16°C that was accompanied by increased expression of *PR1* **(Figure 1-figure supplement 4)**. This observation provides evidence for a functional link between *MHA2*/*SBT2.2* and *ACD6* activity.

MHA1 and its paralog *MHAL* define a new gene family encoding small proteins

The SNP with the highest QTL LOD score, at the locus that explained about 40% of the necrosis variation in the Ty-0 x Est-1 F_2 population, was within 50 kb of the best genome-wide GWA hit, in *MHA1* **(Figure 1D)**. We established Heterogeneous Inbred Families (HIFs) (Loudet et al., 2005) and found that among F_3 and F_6 descendants with reduced or no leaf necrosis, the *MHA1*-Est-1 allele was highly underrepresented **(Figure 1–figure supplement 3C)**. A Near-Isogenic Line (NIL) with the *MHA1*-Est-1 allele was smaller

and suffered from more necrosis than the corresponding NIL with the Ty-0 allele **(Figure 2A)**. *Pseudomonas syringae* pv. tomato (Pst) DC3000 expressing *avrRpt2* has been shown before to respond to differences in *ACD6* activity (Lu et al., 2003), and Pst DC3000 *avrRpt2* grew to lower levels in the NIL with the Est-1 allele, consistent with *MHA1*-Ty-0 suppressing the immunity-enhancing activity of *ACD6*-Est-1 **(Figure 2B)**. Two HIFs allowed us to narrow the QTL interval to a 200 kb region from 22.83 and 23.03 Mb **(Figure 1–figure supplement 3D)**. In the center of this region, at 22.94 Mb, was our top GWA hit, AT1G62045, which encodes a small ~7 kDa protein of 67 amino acids.

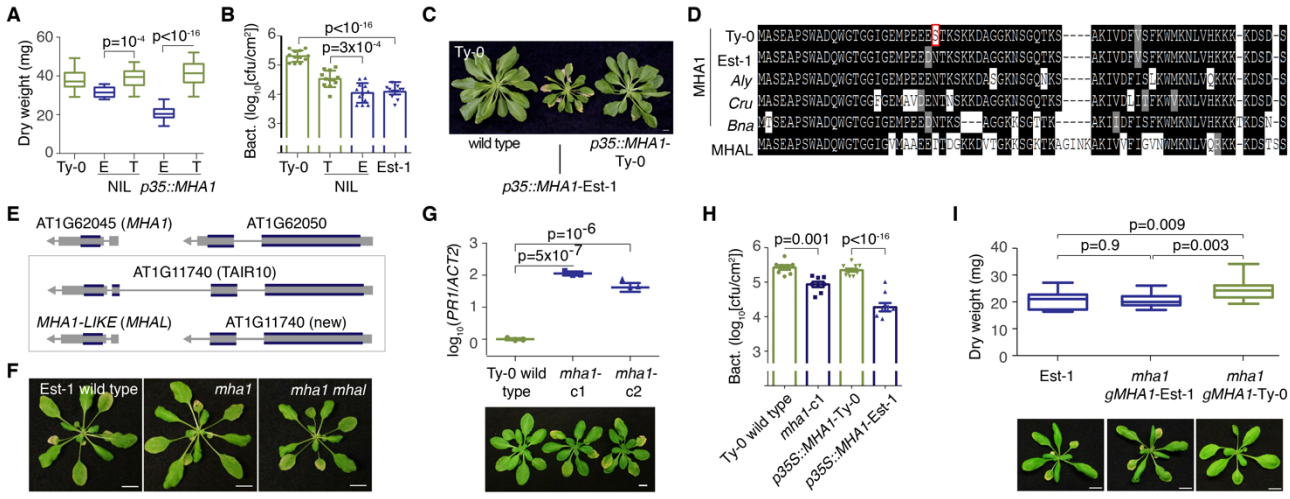

Figure 2. Identification of *MHA1* as a genetic modifier of *ACD6*-Est-1. (A) Dry weight of 4-week-old plants with different *MHA1* alleles. E, Est-1; T, Ty-0. **(B)** Growth of Pst DC3000 *avrRpt2* three days after infection. Four-week old NILs with the *MHA1*-Ty-0 allele support more Pst DC3000 *avrRpt2* growth than those with the Est-1 allele. **(C)** Five-week old *p35S::MHA1* transgenic lines in Ty-0 background grown in 23°C SD. Left, non-transgenic control. Scale bar, 1 cm. **(D)** MHA1 protein alignment among Brassicaceae (*Aly*, *Arabidopsis lyrata*; *Cru*, *Capsella rubella*; *Bna*, *Brassica napus*). MHA1-Ty-0-specific polymorphism highlighted in red. **(E)** Correction of gene annotation of *MHA1-LIKE* (*MHAL*) in the *A. thaliana* reference genome. Paralogous *MHA1* region shown on top. **(F)** CRISPR/Cas9 induced *mha1* and *mha1 mhal* mutants in Est-1 background. **(G)** Top: Accumulation of *PR1* mRNA, as measured by RT-qPCR from three biological replicates each in Ty-0 *mha1* mutants. Bottom: Plant phenotypes. Scale bar, 1 cm. **(H)** Growth of Pst DC3000 *avrRpt2* three days after infection. In the Ty-0 background, overexpression of the *MHA1*-Est-1 allele, but not of the *MHA1*-Ty-0 allele, reduces DC3000 *avrRpt2* growth, similar to inactivation of *mha1* in this background. **(I)** Transgenic Est-1 *mha1* mutants containing genomic *MHA1* fragments from Est-1 or Ty-0. Top, Leaf biomass of 4-week-old plants. *p*-values from Tukey's HSD test. Bottom: Plant phenotypes. Scale bar, 1 cm.

To directly confirm that *MHA1* could suppress *ACD6*-Est-1 activity, we overexpressed in the Ty-0 background the *MHA1* alleles of Ty-0 and Est-1, which differ in two adjacent codons, with one of these causing a non-conservative change from asparagine to serine due to the top GWA SNP. Overexpression of *MHA1*-Ty-0 had no apparent effects on plant morphology (21 T_1 plants), while *MHA1*-Est-1 caused strong leaf necrosis and reduced size in 13 out of 15 T_1 individuals **(Figure 2C)**. These results not only supported the identification of AT1G62045 as *MHA1*, but also suggested that activity of the *MHA1*-Ty-0 allele is compromised relative to the *MHA1*-Est-1 allele. *MHA1* homologs are found in many dicotyledonous plant species, and alignment of the predicted protein sequences told us that other Brassicaceae typically encode the asparagine corresponding to the Est-1 variant, which is representative of the major *A. thaliana* allele **(Figure 2D)**. Finally, because *ACD6* is an immunity regulator, we wondered whether there was any

evidence for its genetic interactor *MHA1* having a role in defense. Consultation of an expression atlas (Winter et al., 2007) revealed that *MHA1* expression was elevated when plants are infected with the bacterium Pst DC3000 expressing *avrRpm1* or with the fungus *Botrytis cinerea*.

In the *A. thaliana* reference genome, *MHA1* and the adjacent gene AT1G62050 are paralogous to the 3' and 5' portions of another gene on chromosome 1, AT1G11740. This gene model appears to be mis-annotated, as public RNA-seq data and RT-PCR analyses indicated that the gene model erroneously fuses two independent genes that are paralogs of *MHA1* and AT1G62050, respectively **(Figure 2E, Figure 2–figure supplement 1A-D)**. We named the *MHA1* paralog *MHA1-LIKE* (*MHAL*).

Genetic characterization of the *MHA1* paralog *MHAL*

To determine the function of *MHA1* and its paralog *MHAL* in regulating *ACD6* activity, we used CRISPR/Cas9 genome editing (Wu et al., 2018) to mutate both genes in Est-1, which has the hyperactive *ACD6* allele. Both *mha1* and *mha1 mhal* double mutants continued to show typical *ACD6*-Est-1-induced necrosis, suggesting that *MHA1* and *MHAL* do not simply act downstream of *ACD6* **(Figure 2F, Figure 2–figure supplement 1E,F)**.

Surprisingly, even though the Ty-0 allele of *MHA1* carried a nonsynonymous substitution that affected a conserved asparagine **(Figure 2D)**, consistent with this allele having reduced or no activity, its inactivation led to leaf necrosis and greatly increased *PR1* expression in Ty-0 **(Figure 2G)**. This was surprising because similar effects were seen when we overexpressed *MHA1*-Est-1 in Ty-0 **(Figure 2C,H)**, suggesting that the Est-1 allele, rather than the Ty-0 allele, was the functional allele. Introduction of a genomic copy of *MHA1*-Ty-0 into Est-1 *mha1* mutants suppressed leaf necrosis and increased biomass, in agreement with this allele interfering with the action of *ACD6*-Est-1 **(Figure 2I)**. Together, these data pointed to *MHA1*-Ty-0 as a gain-of-function allele that acts as a negative regulator of *ACD6*-Est-1 activity in both necrosis and pathogen protection, with the standard allele, *MHA1*-Est-1, masking the action of *MHA1*-Ty-0, even though *MHA1*-Est-1 is not required for *ACD6*-Est-1 activity. Overexpression of either *MHA1*-Ty-0 or *MHA1*-Est-1 did not have obvious effects in a Col-0 background, nor did it appear to modify the phenotype of the laboratory-induced *acd6*-1 gain-of-function allele.

The unusual relationship between the Ty-0 and Est-1 alleles suggested that the functional interaction between *MHA1* and *ACD6* is perhaps complicated by the presence of the *MHAL* paralog, even though the absence of a clear effect on *ACD6*-Est-1 activity in the *mha1 mhal* double mutant had not pointed to *MHA1* and *MHAL* being simply redundant. To gain first insights into *MHAL* function, we compared the effects of overexpressing *MHA1* and *MHAL* in the reference accession Col-0, which has the standard *ACD6* allele, which does not cause necrosis. Neither *MHA1*-Est-1 nor *MHA1*-Ty-0 overexpression had obvious effects in Col-0, although the *MHA1*-Est-1 slightly increased expression of *PR1* **(Figure 3A)**. In contrast, overexpression of *MHAL*, which does not show allelic variation in amino acid sequence between Col-0, Est-1 and Ty-0, caused strong necrosis and dwarfing at 16°C in 24 out of 30 T_1 plants **(Figure 3B)**. The effects at 23°C were milder **(Figure 3–figure supplement 1A)**, which can be at least partially attributed to reduced accumulation of the protein at the higher temperature, as demonstrated with plants overexpressing an

MHAL-GFP fusion **(Figure 3–figure supplement 1B)**. The temperature sensitivity of the *MHAL* overexpressors suggested that *MHAL* can enhance *ACD6* activity, since it resembled the behavior of *acd6*-1 gain-of-function mutants, which also show enhanced necrosis at 16°C compared to the standard temperature of 23°C **(Figure 3B, Figure 3–figure supplement 1A)** (Todesco et al., 2014).

Since *ACD6* is both a regulator and effector of SA responses (Lu et al., 2003; Rate et al., 1999; Tateda et al., 2014; Zhang et al., 2014), we were interested in the relationship between ACD6 and the EDS1/NRG1/ADR1 node of lipase-like proteins and so-called helper NLRs (hNLRs), a convergence point of both ETI and PTI signaling that controls both SA-dependent and -independent defenses (Cui et al., 2017; Lapin et al., 2020; Pruitt et al., 2020; Sun et al., 2020; Wu et al., 2019). To test the requirement of hNLRs for *MHAL* activity, we overexpressed *MHAL* in plants carrying different combinations of mutations in the *ADR1* and *NRG1* subfamilies of hNLRs (Wu et al., 2019). *MHAL*-induced necrosis and dwarfism were partially suppressed in *nrg1* triple mutants and fully suppressed in *adr1 nrg1* sextuple mutants **(Figure 3C)**, indicating that hNLRs are redundantly required for *MHAL* function. While the redundancy between the two subfamilies was in agreement with other findings (Lapin et al., 2020; Pruitt et al., 2020; Sun et al., 2020; Wu et al., 2019), the stronger suppression of the *MHAL* overexpression effects was somewhat surprising, since it is the *ADR1* subfamily that has been primarily linked to SA signaling (Bonardi et al., 2011; Castel et al., 2019). Additional genetic analysis confirmed that *MHAL* overexpression defects were dependent on SA accumulation, as the phenotype was completely suppressed by expression of the bacterial salicylate hydroxylase gene bacterial *nahG* gene, which converts SA to catechol (Gaffney et al., 1993), similar to what has been reported for other lines with increased *ACD6* activity (Lu et al., 2005, 2003; Rate et al., 1999; Todesco et al., 2014, 2010) **(Figure 3–figure supplement 2)**. Mutations in *NPR1*, which partially attenuates SA signaling, had more modest effects on the phenotype of *MHAL* overexpressors, similarly to what has been reported for *acd6*-1 mutants (Rate et al., 1999) **(Figure 3–figure supplement 2)**.

To test the genetic requirements for the semi-lethal effects of *MHAL* overexpression in an unbiased manner, we mutagenized *MHAL* overexpressors in the Col-0 background with ethyl methanesulfonate. When we sequenced the genomes of 72 M_3 *suppressor of MHAL* (*somhal*) lines, we found multiple mutations in *RST1* and mutations *XRN4*, two loci that prevent transgene silencing (Gazzani et al., 2004; Lange et al., 2019; Li et al., 2019) **(Table 3)**. The most often mutated locus was *ACD6*, in 37 of the 72 suppressor lines, with 28 distinct variants **(Figure 3D, Table 3)**. Four mutations in *ACD6* caused non-synonymous substitutions that have been reported as intragenic suppressors of the *acd6*-1 gain-of-function allele (Lu et al., 2005), consistent with them being loss-of-function alleles. We confirmed that the *ACD6* locus co-segregated with suppression of *MHAL*-associated necrosis for one of the mutant lines **(Figure 3E)**. In *somhal* lines without mutations in *ACD6*, strong necrosis was restored in F_1 progeny from a cross to the *acd6*-2 loss-of-function mutant, indicating that the transgene itself was not mutated and that the suppressor mutations were apparently at other loci **(Figure 3F)**. Final validation for *ACD6* being essential for the effects of *MHAL* overexpression was obtained with the known *acd6*-2 loss-of-function allele, which suppressed the *MHAL* overexpression phenotype as well (25 T_1 individuals) **(Figure 3G, Figure 3–figure supplement 3A)**. In contrast, the *acd6*-1 gain-of-function mutation greatly enhanced the phenotype of *MHAL* overexpressors

(15 T_1 individuals). At 23°C, *acd6*-1 *p35S::MHAL* plants resembled *MHAL* overexpressors without the *acd6*-1 allele grown at 16°C **(Figure 3G, Figure 3–figure supplement 3A)**.

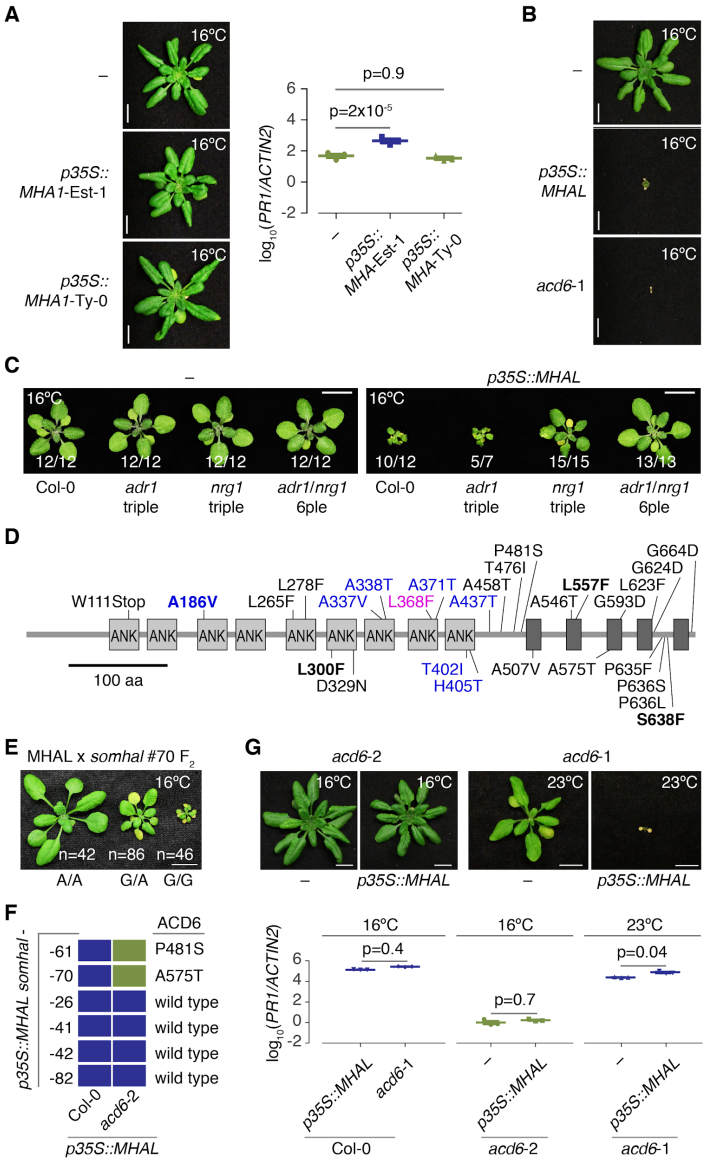

Figure 3. Functional divergence of *MHA1* and *MHAL* in causing *ACD6*-dependent necrosis. **(A)** Transgenic plants overexpressing *MHA1*-Est-1 or *MHA1*-Ty-0 alleles in the Col-0 reference background, and accumulation of *PR1* mRNA, as measured by qRT-PCR from three biological replicates each. *p*-values from Tukey's HSD test. **(B)** Transgenic plants overexpressing *MHAL* in Col-0. *acd6*-1 shown for comparison. **(C)** Effects of mutating hNLR genes in Col-0 or *MHAL* overexpressors. Numbers indicate fractions of T_1 transgenic plants with the phenotype shown. **(D)** Map of 28 EMS-induced *somhal* mutations in *ACD6* identified as suppressors of *MHAL*-induced necrosis. Numbers indicate codons. Four mutations in bold are identical to ones that have been isolated before as intragenic suppressors of the *acd6*-1 gain-of function allele (Lu et al., 2005). Blue residues are identical in two out of three mammalian TRP proteins (TRPA1, NOMPC, TRPV6), magenta residue in all three. Ankyrin repeats (ANK) annotated; predicted transmembrane helices shown as black boxes. **(E)** Co-segregation between the polymorphism in $acd6^{575}$ with *p35S::MHAL*-associated necrosis in a backcross F_2 population derived from *somhal* suppressor mutant #70 and the parental *p35S::MHAL* line. "A" corresponds to the *ACD6* wild-type allele. **(F)** Phenotypes of F_1 progeny from crosses of different *somhal p35S::MHAL* plants to Col-0 *p35S::MHAL* and *acd6*-2 *p35S::MHAL* plants. Dark green indicates absence of necrosis (no complementation of *somhal p35S::MHAL* phenotype), and dark blue necrosis (complementation). *ACD6* amino acid changes shown on the right. **(G)** Transgenic *acd6*-2 and *acd6*-1 plants overexpressing *MHAL*, and accumulation of *PR1* mRNA, as measured by qRT-PCR from three biological replicates each. *p*-values from Tukey's HSD test. Scale bars, 1 cm (A, B, E, G), or 0.5 cm (C).

Together, the experiments with *MHAL* overexpressors and *acd6* loss- and gain-of-function alleles in the Col-0 background indicated that *MHAL* and *ACD6* depend on each other's activities. This conclusion seemed, however, inconsistent with the finding that the hyperactive *ACD6*-Est-1 allele appeared to function in an *MHAL*-independent manner, since the inactivation of *MHAL* (and *MHA1*) did not suppress the *ACD6*-Est-1 phenotype **(Figure 2B)**. We confirmed the mutual independence by overexpressing *MHAL* in an *ACD6*-Est-1 background. Not only was the *ACD6*-Est-1 phenotype not enhanced by *MHAL* overexpression, but the severe *MHAL* overexpression phenotype at 16°C was suppressed in Est-1 and a NIL with the *ACD6*-Est-1 allele **(Figure 3–figure supplement 3B)**, indicating genetic interaction of *MHAL* with the standard *ACD6*-Col-0, but not the *ACD6*-Est-1 allele. Note that the phenotype of *ACD6*-Est-1, in contrast to that of *acd6*-1, is not enhanced by lower temperature (Todesco et al., 2014, 2010), which distinguishes *ACD6*-Est-1

from many other autoimmunity mutants (van Wersch et al., 2016). These observations were further complicated by the finding that *MHA1* in the Ty-0 background suppresses *ACD6*-Est-1 activity, indicating that *ACD6*-Est-1 does not act independently of *MHA1*. On the other hand, not only did GFP-MHAL accumulate to higher levels in *p35S::GFP-MHAL* plants at lower temperature **(Figure 3–figure supplement 1B)**, but *MHAL* RNA expression in *acd6*-1 was also enhanced at lower temperature. In addition, GFP-MHAL accumulated to higher levels in an *acd6*-1 background **(Figure 3–figure supplement 1C)**. Together, these observations provide a potential explanation for the more severe *acd6*-1 phenotype under lower temperature **(Figure 3–figure supplement 1A)**.

Characterization of MHA1 and MHAL proteins

To begin to find possible explanations for the puzzling complexity in genetic interactions between *ACD6*, *MHA1* and *MHAL*, we began to characterize protein-protein interactions. Split-luciferase complementation assays in *Nicotiana benthamiana* indicated that ACD6-Est-1 protein can interact with both MHA1 and MHAL **(Figure 4A)**. Co-immunoprecipitation (co-IP) with material extracted from protoplasts overexpressing tagged proteins indicated that ACD6-Col-0 interacts with both MHAL than with MHA1 **(Figure 4B)**. *ACD6* encodes a transmembrane protein with ankyrin repeats (Lu et al., 2003; Zhang et al., 2014), which are obvious candidates for the interaction of ACD6 with other proteins. We therefore tested whether MHAL and ACD6-Col-0 might directly bind to each other using *in vitro* GST pull-down assays. We did detect such binding **(Figure 4C)**, in agreement with the protoplast co-IP results **(Figure 4B)**. In all three assays, split-luciferase, GS pull-down and co-IP, MHAL tended to produce a stronger signal than MHA1, but more quantitative methods will be required to determine whether these apparent differences are significant. Finally, we examined the subcellular localisation of a GFP fusion to MHA1-Est-1 in Ty-0. In root cells, GFP signal was found both in the cytoplasm and at the membrane **(Figure 4D)**. After plants had been treated for 45 minutes with 10 µM brefeldin A (BFA), an endocytosis inhibitor, MHA1-GFP accumulated in BFA bodies that co-stained with the endocytic tracer FM4-64, which suggested that MHA1-GFP recycles between the plasma membrane and endosomal compartments, similar to many other plant plasma-membrane proteins (Contento and Bassham, 2012) **(Figure 4E)**. Subcellular fractionation indicated that both MHA1-GFP and MHAL-GFP proteins were enriched in microsomes **(Figure 4F,G)**, similar to ACD6-1 protein (Zhang et al., 2014) **(Figure 4H)**. The similar subcellular localization of MHA1 and ACD6 was in agreement with direct interaction of the proteins.

Given the differential interaction of MHA1 and MHAL proteins with ACD6 ankyrin repeats, and the observed genetic interactions, in which *MHAL* overexpression did not affect *ACD6*-Est-1 activity, while *MHA1*-Ty-0 suppressed *ACD6*-Est-1 effects, we developed the following hypothesis for the MHA1/MHAL interaction with ACD6: First, MHAL enhances activity of the standard form of ACD6 (as found in Col-0); such an enhanced activity could provide additional feedforward regulation of *ACD6* in response to pathogen challenge, as both enhanced *ACD6* activity and treatment of plants with a bacterial pathogen increased *MHAL* mRNA accumulation **(Figure 3–figure supplement 1E)**. Second, the amino acid replacements in the transmembrane portion of ACD6-Est-1 that are causal for its increased activity (Todesco et al., 2010) alter

the conformation of ACD6-Est-1, such that it no longer requires binding of MHAL to its ankyrin repeats for increased activity. ACD6-Est-1 can, however, be bound by MHA1-Ty-0 **(Figure 4A)**, which in turn interferes with ACD6-Est-1 activity.

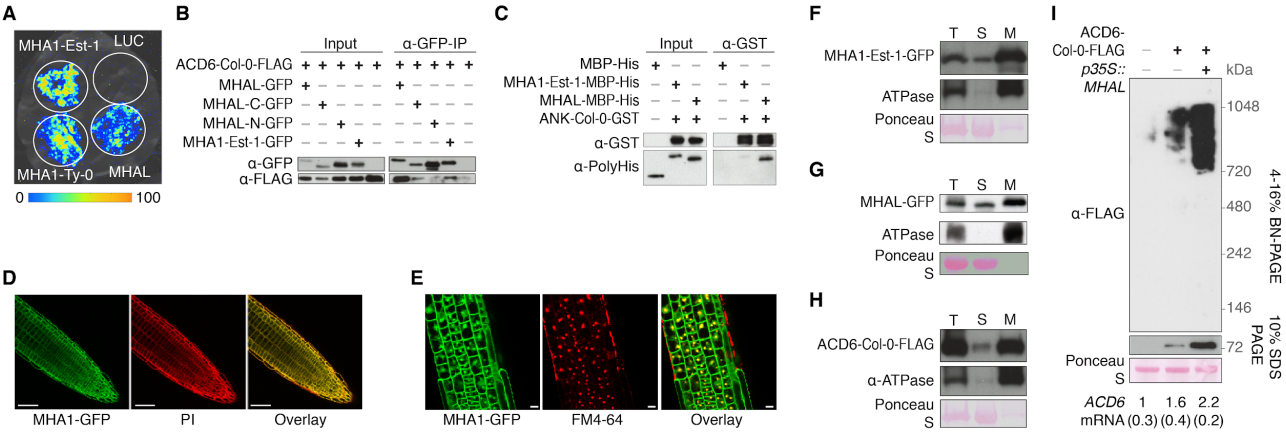

Figure 4. MHAL enhances ACD6 accumulation and formation of ACD6 complexes. (A) Split-luciferase complementation assays indicating interaction of ACD6-Est-1 with both MHA1 and MHAL in *Nicotiana benthamiana*. **(B)** Co-IP assays with *A. thaliana* Col-0 protoplasts showing interaction of ACD6-Col-0 with MHA1 and both N- (residues 1-34) and C-terminal (residues 20-72) fragments of MHAL. **(C)** GST pull-down assay demonstrating interaction of the ANK domains of ACD6-Col-0 with MHAL and, less strongly, with MHA1. **(D)** Localization of MHA1-Est-1-GFP in root cells; cell walls were stained with propidium iodide (PI). Scale bar, 50 µm. **(E)** Change of subcellular localization of MHA1-Est-1-GFP in response to 10 µM BFA (45 min after treatment). Plasma membranes stained with FM4-64. Scale bar, 50 µm. **(F-H)** Subcellular microsomal fractionation of **(F)** *p35S::MHA1-GFP*, **(G)** *p35S::GFP-MHAL* and **(H)** *pACD6::ACD6*-Col-0-*FLAG* transgenic plants. T, total; S, supernatant; M, microsomal fraction. **(I)** BN-PAGE and SDS-PAGE showing that *MHAL* overexpression enhances accumulation and complex formation of ACD6. Increased RNA levels due to the presence of the *ACD6*-Col-0-*FLAG* transgene, as measured by qRT-PCR, indicated as means (± SD) at the bottom. Experiments were repeated twice with similar results.

To understand how MHAL enhances the activity of ACD6 protein, we investigated ACD6 accumulation and complex formation in *A. thaliana* plants using Blue Native polyacrylamide gel electrophoresis (BN-PAGE), which was previously used to show that ACD6 exists in complexes of around 700-800 kDa (Zhang et al., 2017, 2014). Overexpression of MHAL increased the total levels of ACD6 and that of large ACD6 complexes **(Figure 4I)**, similar to what has been shown for the mutation in *acd6*-1, which, like MHAL overexpression, enhances ACD6 activity (Lu et al., 2003; Zhang et al., 2014). The higher levels of ACD6 complexes in MHAL overexpressors were apparently mainly due to increased accumulation of ACD6 protein, rather than *ACD6* RNA **(Figure 4I)**.

Ca^{2+} and *ACD6* triggered immunity

That ACD6 activity was modulated by molecules from both intracellular (MHA1 and MHAL) and extracellular (MHA2) compartments, led us to hypothesize that ACD6, a membrane-associated protein with multiple predicted transmembrane domains, facilitates the transport of signalling molecules across the plasma membrane. To determine whether ACD6 might be structurally similar to other proteins with such activities, we performed HHpred profile Hidden Markov Model searches (Zimmermann et al., 2018) and found multiple excellent hits to transient receptor potential (TRP) channels from animals and fungi, which regulates ion flux

in response to stimuli ranging from heat to natural products and proinflammatory agents (Julius, 2013; Venkatachalam and Montell, 2007) **(Figure 5–figure supplement 1A)**. Alignments revealed extensive similarity of ACD6 and TRP family ankyrin repeats **(Figure 5–figure supplement 1B)**, but not to the transmembrane domains (Huffer et al., 2020). Out of 12 loss-of-function mutations mapping to the ACD6 ankyrin repeats, eight of the affected residues were identical in alignments to at least two out of the three top HHPred hits, fly NOMPC, human TRPA1, and rat TRPV6 **(Figure 3D)**. The *A. thaliana* genome encodes over 100 ankyrin repeat proteins, with many of them having transmembrane domains (Becerra et al., 2004). ACD6 protein has been predicted to contain up to seven transmembrane domains (Lu et al., 2003), but we could reliably identify only five transmembrane domains (Krogh et al., 2001). Furthermore, homology modeling did not suggest that the structure of the ACD6 transmembrane domains is consistent with those of TRP channels, which have six transmembrane helices, with helices 5 and 6 forming the ion pore in a functional TRP multimeric ion channel (Julius, 2013; Venkatachalam and Montell, 2007) **(Figure 5–figure supplement 1C)**.

Given the similarity of ACD6 and TRP channel ankyrin repeats, we proceeded to investigate potential channel activity of ACD6 using African clawed frog (*Xenopus laevis*) oocytes. We observed small inward currents after addition of external Na+ in oocytes expressing ACD6 variants, but the difference to the control was only statistically significant for the ACD6-1 gain-of-function variant.

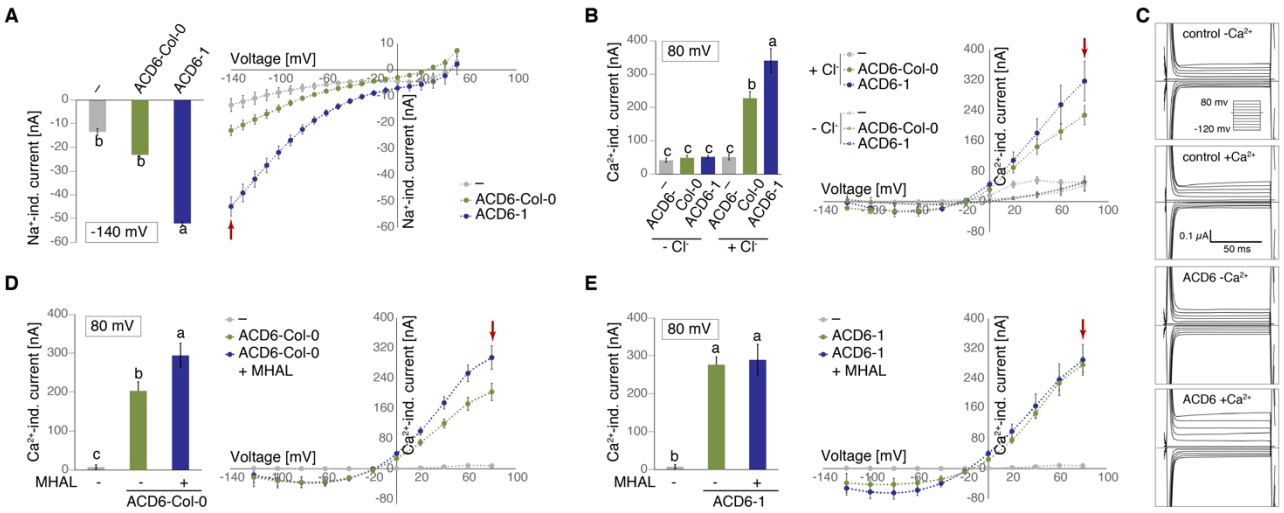

Figure 5. Stimulation of ion channel activity by ACD6 in oocytes and enhancement by MHAL. **(A)** Currents induced by 10 mM Na^+ in *Xenopus laevis* oocytes kept in choline chloride dominated solution and expressing ACD6-Col-0 or ACD6-1. **(B)** Currents induced by 10 mM Ca^{2+} in ACD6 variants-expressing oocytes in the presence or absence of Cl^-. On the right, the data points for ACD6-1 without Cl^- are obscured by the ACD6-Col-0 data points without Cl^-. **(C)** Representative original current traces from ACD6-Col-0 recordings (B) in Cl^--containing solution in the presence and absence of Ca^{2+}. Voltage protocol and scale for all traces are indicated. **(D, E)** MHAL enhancement of Ca^{2+}-induced currents in oocytes expressing ACD6-Col-0 (C), but not ACD6-1 (D). Left, currents at -140 mV (A) or 80 mV (B, C, D). Right, current-voltage relations of a representative oocyte batch; red arrows indicate voltages shown for comparisons on the left. Shown are means (n>3 [A], or n>5 [B, C, D]) ± SE; letters indicate significantly different groups (p<0.01 [A, B], p<0.05 [C, D]; post hoc Tukey's HSD). Controls ("–"): non-injected oocytes.

Direct observation of Ca^{2+} influx is hampered in *Xenopus* oocytes by the presence of endogenous Ca^{2+}-activated chloride channels. These are stimulated by the accumulation of intracellular Ca^{2+} and typically mask small ionic currents from Ca^{2+} influx. However, these endogenous channels can be used as quantitative readout for channel-mediated Ca^{2+} influx by foreign functional Ca^{2+} channels (Hartzell et al., 2005; Tian et al., 2019). When we raised the external Ca^{2+} concentration in our experiments with oocytes expressing the standard ACD6-Col-0 or gain-of-function ACD6-1 variant, we observed ionic currents that resembled Ca^{2+}-activated chloride currents in their current-voltage relationship; these currents were lost upon removal of external chloride **(Figure 5A,B)**. Consistent with the role of MHAL as an ACD6 activator in plants, MHAL could further enhance these currents in ACD6-Col-0 expressing oocytes, though not in ACD6-1 expressing oocytes **(Figure 5C,D)**. Together, these results showed that ACD6 stimulates ion channel activity when expressed in oocytes, perhaps with ACD6 itself as a Ca^{2+}-permeable ion channel.

Since ACD6 could stimulate Ca^{2+} influx in oocytes, we further tested whether Ca^{2+} is required for *ACD6*-triggered immunity. To this end, we cultured the gain-of-function mutant *acd6*-1 in a hydroponic system that contained either 1.5 or 0.1 mM external Ca^{2+}. Similar to the Ca^{2+} channel mutant *death, no defense1* (*dnd1*-1) *(Tian et al., 2019)*, we found that depletion of Ca^{2+} attenuated signs of autoimmunity and expression of *PR1* in *acd6*-1 **(Figure 6A)**. We also tested the effects of external Ca^{2+} on the increased growth of Pst DC3000 *hrcC*- bacteria, which elicit PTI, in *acd6*-2 loss-of-function mutants (Tateda et al., 2014). Consistent with Ca^{2+} being required for *ACD6* activity, the difference between *acd6*-2 mutants and wild-type plants disappeared when external Ca^{2+} was depleted **(Figure 6B)**.

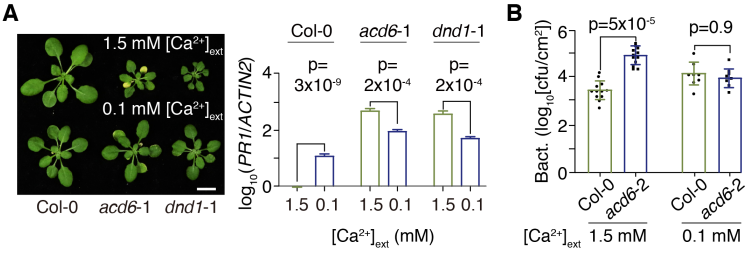

Figure 6. Ca^{2+} is essential for *ACD6* triggered autoimmunity and PTI responses. (A) Left, rosettes of 3-week-old plants grown with different concentrations of external Ca^{2+}. Right, accumulation of *PR1* mRNA, as measured by qRT-PCR from three biological replicates each. The experiment was repeated twice with similar results. Scale bar, 1 cm. **(B)** Growth of Pst DC3000 *hrcC*- bacteria after 4 days of infection in plants cultured with different concentrations of external Ca^{2+}. The experiment was repeated twice with similar results. *p*-values from Tukey's HSD.

Discussion

Epistasis has been proposed as one of the explanations for missing heritability in genetic mapping studies (Eichler et al., 2010; Mackay, 2014; Manolio et al., 2009), with particular challenges presented by alleles that on their own do not seem to have obvious phenotypic effects, a phenomenon known as cryptic genetic variation (Gibson and Dworkin, 2004; Paaby and Rockman, 2014). Here, we have demonstrated the power of GWA studies of sub-populations carrying specific alleles to identify cryptic modifiers, resulting in the discovery of a family of small peptides that modulate the activity of the immune regulator ACD6 by binding to its ankyrin repeats.

Our study began with *A. thaliana* accessions carrying the naturally hyperactive *ACD6*-Est-1 allele, whose phenotypic effects in different genetic backgrounds depend on two unlinked loci, *MHA1* and *MHA2*.

Suppressor alleles at *MHA1* and *MHA2* are more likely to be found in *ACD6*-Est-1 carriers than in individuals with the standard *ACD6* allele, suggestive of selection for specific combinations of *ACD6*/*MHA1*/*MHA2* alleles. Follow-up studies of *MHA1* and its paralog *MHAL* in turn identified a new gene family that regulates plant immunity and led to new insights into the biochemical activity of ACD6. Because *MHA1* and *MHAL* encode only small proteins, they constitute small targets for mutagenesis and thus would not have been easily found in conventional genetic screens.

We discovered that the ankyrin repeats of ACD6 are similar in sequence to those of mammalian TRP proteins, and that as TRP proteins, ACD6 functions can stimulate ion flux across membranes **(Figure 5–figure supplement 1)**. There is enormous knowledge on the structure and function of TRP ion channels, providing potential models for understanding the activity of ACD6 (Huffer et al., 2020; Julius, 2013; Venkatachalam and Montell, 2007). Similar to a subset of TRP proteins, ACD6 can apparently be regulated through its ankyrin repeats by small ligands, the MHA1 and MHAL proteins, with MHAL enhancing the activity of both the standard ACD6 protein and its derivative mutant ACD6-1 protein, but not of the ACD6-Est-1 variant. In contrast, MHA1-Ty-0, but not the standard MHA1 protein, can suppress activity of the ACD6-Est-1 variant **(Figure 5–figure supplement 2A)**.

TRP channels typically function as tetramers, with two membrane-spanning helices from each subunit contributing to the ion channel pore (see (Huffer et al., 2020) for a recent compilation of TRP channel structures). ACD6 is also found in a large complex (Zhang et al., 2017, 2014) **(Figure 4I)**, but the size of this complex is substantially greater than that of a simple tetramer, suggesting either a higher oligomeric state or association with additional proteins. Several TRP channels can form heteromultimers, with heteromultimers often having different activities than the homomultimers (Venkatachalam and Montell, 2007). In *A. thaliana*, combinations of natural *ACD6* alleles, including those from the Mir-0 and Se-0 accessions, can lead to increased ACD6 hyperactivity in F_1 hybrids relative to either parent (Świadek et al., 2016; Todesco et al., 2014) **(Figure 5–figure supplement 2B)**, compatible with a scenario in which the variants assemble into heteromultimers in the F_1 hybrids that have different properties than the respective homomultimers.

Also similar to *ACD6*, gain-of-function mutations in TRP channel genes are common, with many of these having been identified as variants underlying human genetic diseases (Myers et al., 2008b). *ACD6* itself was originally discovered based on the gain-of-function, hyperactive *acd6-1* mutant allele induced in the lab (Rate et al., 1999). A hyperactive natural allele, *ACD6*-Est-1, was subsequently found to be common in natural populations of *A. thaliana* (Todesco et al., 2010). The Mir-0/Se-0 combination described above can also be considered as a gain-of-function situation. In all four alleles, the sequences responsible for increased activity are found in the predicted transmembrane portion of ACD6 **(Figure 5–figure supplement 2B)**. While some gain-of-function mutations in TRP channels affect either the N-terminal portions including the ankyrin repeats or the C-terminal portions, many alter amino acids in the transmembrane domain **(Table 4)**. This is significant, because, as in ACD6, the overall length of the transmembrane domains is typically much shorter than the length of the other domains, making for a smaller mutational target.

TRP channels can integrate inputs consisting of different stimuli or ligands, and the opposite effects of MHA1 and MHAL on ACD6 activity are reminiscent of the effects of different ligands on TRPV1 activity (Lishko et al., 2007). Whether MHA1 is a bona fide regulator of ACD6 remains unclear, because we could so far only show that a natural gain-of-function allele acts in a dominant negative fashion to attenuate activity of the *ACD6*-Est-1 allele **(Figure 2F)**. Inactivation of *MHA1* did not seem to affect *ACD6* activity **(Figure 2F)**. It is conceivable that MHA1 is a regulator of an ACD6 homolog; *A. thaliana* genomes encode about half a dozen proteins with close similarity to ACD6 in both the ankyrin repeats and transmembrane domains. Redundancy among these proteins may also explain why inactivation of *ACD6* has relatively minor consequences (Lu et al., 2003) compared to the pronounced phenotypic effects resulting from *ACD6* hyperactivity or MHAL overexpression (Rate et al., 1999; Świadek et al., 2016; Todesco et al., 2014, 2010) (this work). On the other hand, the effects of MHAL overexpression seem to be entirely dependent on ACD6, pointing to an exclusive relationship between MHAL and ACD6. It may appear surprising that MHAL enhances accumulation of an ACD6 complex, rather than merely regulating its activity, but increased accumulation of ACD6 has also been observed in *acd6*-1 mutants (Zhang et al., 2014), consistent with positive feedback regulation of ACD6. A possibility is that MHAL does not directly regulate ACD6 activity, but instead stabilizes ACD6 via other membrane-resident proteins with which ACD6 associates (Tateda et al., 2014; Zhang et al., 2017, 2014). Indeed, ACD6 has been shown to be regulated by protein degradation in the cytoplasm (Zhang et al., 2014).

Although the ankyrin repeats of TRP proteins are similar to those of ACD6 and related plant proteins, it is unclear whether the ACD6 transmembrane domains adopt a similar topology as TRP channels and therefore whether it acts as an ion channel itself **(Figure 5–figure supplement 1C)**. Nevertheless, ACD6 can stimulate Ca^{2+} influx in a heterologous system **(Figure 5)** and several of its effects *in planta* require Ca^{2+} **(Figure 6)**. Ca^{2+} influx from extracellular stores is an early event in the host response to pathogens, with relatively well characterized downstream steps. One of the earliest cellular responses to PAMPs is the rapid increase of cytoplasmic Ca^{2+} levels, indicating that Ca^{2+} channels are intimately associated with PTI. In agreement, genetics has implicated cyclic nucleotide-gated channel (CNGCs) in this process for a while, and at least one of these CNGCs is a functional Ca^{2+} channel whose activity is regulated by pathogen- and damage-associated molecular patterns (PAMPs/DAMPs), such as lipopolysaccharide (LPS), flagellin 22 (flg22) and plant elicitor peptide 3 (Pep3) (Bredow and Monaghan, 2019; Ma and Berkowitz, 2007; Moeder et al., 2019; Qi et al., 2010; Seybold et al., 2014; Tian et al., 2019). PAMPs also regulate activity of Ca^{2+} channels from the OSCA family, which are important in stomata-dependent immunity (Thor et al., 2020).

Similar to the induced *acd6*-1 and the natural *ACD6*-Est-1 alleles, mutations in genes for several plant Ca^{2+} channels and transporters, including the ACA1 and ACA4 Ca^{2+}-ATPases, the CAX1 and CAX3 vacuolar H^+/Ca^{2+} transporters, and the CNGC2/DND1 and CNGC4/DND2 Ca^{2+} channels, can cause autoimmunity (Cheng et al., 2005; Clough et al., 2000; Hilleary et al., 2020; Tian et al., 2019). We propose that ACD6 modifies PAMP-triggered Ca^{2+} signals, supported by the finding that the Ca^{2+} environment affects both autoimmunity in *acd6*-1 gain-of-function mutants and the proliferation of PTI-inducing Pst DC3000 *hrcC*- bacteria in *acd6*-2 loss-of-function mutants **(Figure 6)**. Ca^{2+} likely also plays a role in ETI, as *cngc2/dnd1*

mutants are impaired in the response to both avirulent and virulent bacterial pathogens (Clough et al., 2000). Moreover, Ca^{2+} channel blockers suppress cell death activated by the NLRs RPM1 and ZAR1 (Grant et al., 2000; J. Wang et al., 2019). *ACD6* in turn has been genetically linked to the NLR SNC1 (Zhu et al., 2018) and to helper NLRs of the ADR1 and NRG1 families **(Figure 3C and Figure 5–figure supplement 2)**. Our discovery of the MHA1/MHAL family of peptides strengthens the case for ACD6 being a dynamic immune regulator, since MHAL, which can activate strong, ACD6-dependent immune responses, appears to be transcriptionally induced upon pathogen infection **(Figure 3–figure supplement 1E)**.

Several other ACD6-related transmembrane domain proteins with ankyrin repeats are involved in plant immunity. Cereals encode a series of ACD6 related proteins (Vo et al., 2015), and one of these has been implicated in resistance to the smut fungus *Ustilago maydis* in maize (Zhang et al., 2019). In *A. thaliana*, BDA1, predicted to have four instead of six transmembrane segments as in ACD6 and TRP proteins, is required for activity of the receptor-like protein SUPPRESSOR OF NPR1-1, CONSTITUTIVE 2 (SNC2) in plant immunity (Yang et al., 2012). As with the induced *acd6*-1 gain-of-function allele and the natural hyperactive *ACD6* alleles, a mutation causal for *BDA1* gain-of-function activity maps to the transmembrane domain. Whether any of these ACD6 homologs depend at least in part on small peptide ligands remains to be determined.

Finally, it will be worth investigating in more detail the role of the *ACD6* modifier *MHA2*, which encodes an extracellular subtilase **(Figure 1 and Figure 1–figure supplement 4)**. Plant genomes encode large numbers of subtilases, several of which play a role in biotic defense (Schaller et al., 2018). This may include processing of other extracellular proteases required for defense (Paulus et al., 2020), or perhaps the generation of danger-associated molecular patterns (DAMPs), which trigger PTI (Ramírez et al., 2013; Reichardt et al., 2018). Of particular interest will thus be to learn whether ACD6 can be directly activated by extracellular signals.

In summary, our results demonstrate a complex set of epistatic relationships between different alleles and paralogs in this system, and positive (ACD6-Est-1 and *acd6*-1, MHAL overexpression) or negative (*MHA1*-Ty-0) gain-of-function activities. Further complexity is added by the aggregate activity in this system being either temperature-sensitive or -insensitive, depending on the *MHAL*-requirement of the *ACD6* allele. The nature of the cryptic modifiers of *ACD6* activity led us to investigate new aspects of the biochemical function of ACD6, which revealed it to be a modulator of ion influx, with ACD6 itself possibly being an ion channel that is regulated by peptides that bind to its intracellular ankyrin repeats. Our findings thus illustrate once more how naturally evolved special alleles, which are unlikely to be recoverable from conventional mutant screens, can provide new insights into fundamental aspects of plant biology.

Materials and methods

Plant material and growth. *Arabidopsis thaliana* accessions **(Table 1)** and *Nicotiana benthamiana* were derived from stocks maintained in the lab. Seeds were germinated and cultivated in growth rooms at a constant temperature of 23°C or 16°C, air humidity at 65%, 16 hr (long days) or 8 hr (short days) day length, under 110 to 140 µmol m^{-2} s^{-1} light provided by Philips GreenPower TLED modules (Philips Lighting GmbH,

Hamburg, Germany) with a mixture of 2:1 DR/W LB (deep red/white mixture with ca. 15% blue) and W HB (white with ca. 25% blue), respectively.

The hydroponic system used for assessing the effects of Ca^{2+} has been described (Vasseur et al., 2019) and was used with minor modifications. In brief, the plants were cultivated on inorganic solid media, and all nutrients were provided through the watering solution. The hydroponic medium contained 1 mM KH_2PO_4, 1 mM $MgSO_4$, 0.25 mM K_2SO_4, 0.1 mM $C_{10}H_{12}FeN_2NaO_8$, micronutrients (50 µM KCl, 30 µM H_3BO_3, 5 µM $MnSO_4$, 15 µM $ZnSO_4$, 1 µM $CuSO_4$, 1 µM $NaMoO_4$), 1 mM NH_4NO_3, 1 mM NH_4Cl, 1 mM KNO_3 and different concentrations of $CaCl_2$ (pH 5.8, adjusted with KOH).

Genome-wide association study (GWAS). Severity of leaf necrosis was scored on an arbitrary scale from 1 to 5 using six biological replicates **(Table 1)**, and GWAS with efficient mixed-model (EMMAX) methods was performed with the easyGWAS web interface (Grimm et al., 2016). The Bonferroni correction with a threshold of 0.05 for multiple testing corresponded to an uncorrected *p*-value of 7.6×10^{-8}. The variance explained (adjusted R^2) by the two loci was estimated using a Generalized Linear Model (GLM) using R (R Core Team, 2019), with necrosis as response variable and the two SNPs targeting the MHA loci as fixed effects with an interaction term.

Linkage mapping in crosses. We scored Ty-0 x Est-1 F_2 individuals for the severity of leaf necrosis on an arbitrary scale from 0.5 to 10. Days to visible leaf necrosis were taken into account as well in this score. We analyzed 798 F_2 individuals, extracted genomic DNA from 190 F_2 individuals with extreme phenotypes (97 with scores of 0.5-3 and 93 with scores of 8.5-10), prepared RAD-seq libraries with barcodes for multiplexing after KpnI digestion (Rowan et al., 2017), and sequenced the samples on a HiSeq2000 instrument (Illumina, San Diego, CA, USA) with 150 bp single-end reads. After de-multiplexing using SHORE (https://sourceforge.net/projects/shore), reads were mapped to the TAIR10 reference genome using BWA-MEM (Li and Durbin, 2009). bcftools (Li et al., 2009) and vcftools (Danecek et al., 2011) were used to call SNPs and generate the final VCF file, which was then processed using R (https://www.r-project.org/) for quality control and for generating a SNP matrix for QTL mapping. Whole-genome linkage analysis was performed using R-qtl (Broman et al., 2003), and LOD scores were calculated under a single-QTL model using the function "scanone" with the expectation-maximization (EM) algorithm.

The LOD score significance threshold was established using 1,000 permutations. To fine map *MHA1*, 8,000 F_3 progeny of F_2 individuals heterozygous at *MHA1* but homozygous in the other three QTL regions were scored for leaf necrosis. We genotyped 1,157 of the F_3 individuals with suppressed leaf necrosis using SSLP markers around *MHA1* **(Table 5).** A Heterogeneous Inbred Family (HIF) (Loudet et al., 2005) was used to establish F_6 generation Near Isogenic Lines (NILs) that differed only in the *MHA1* region.

Phylogenetic analysis of *MHA2* DNA sequences. Eight-seven *MHA2* sequences, extracted from the 1001 Genomes dataset (http://1001genomes.org) (1001 Genomes Consortium, 2016), were used to infer phylogenetic relationships with Maximum likelihood (ML) approaches in MEGA6 (Tamura et al., 2013), using *MHA2's* homolog *SBT2.3* (AT5G44530) as outgroup. Node confidence was estimated with 1,000 bootstrap replications.

Linkage disequilibrium calculation. Genomic regions surrounding *MHA1* and *MHA2* were subsetted from a short read VCF of 1001 Genomes data (1001 Genomes Consortium, 2016) using vcftools version 15.1 (Danecek et al., 2011). Linkage disequilibrium R^2 values were calculated with PLINK version 1.9, with a window of 15 kb and an R^2 threshold of 0.

Transgene-free genome-edited lines. An *A. thaliana* codon-optimized Cas9 (*athCas9*) (Li et al., 2013) was used, with the final *pUBQ10::athCas9:trbcs::gRNA1::gRNA2::mCherry* constructs assembled from six GreenGate modules (Lampropoulos et al., 2013). Module A – *A. thaliana pUBQ10*; B – *A. thaliana* codon-optimized *Cas9*; C – *rbcs* terminator; D and E – sgRNAs **(Table 6)** expressed from *A. thaliana* U6 promoter (Li et al., 2013); F – *pAT2S3::mCherry:tMAS* cassette (Gao et al., 2016) for selection of seeds with or without the transgene. Target regions were PCR amplified using oligonucleotide primers in **Table 7**.

qRT-PCR. RNA was extracted from at least three biological replicates of pooled seedlings using the RNeasy kit (Thermo Fisher Scientific, Waltham, MA, USA), and treated with DNase I (Thermo Fisher Scientific). We used 2 µg of high-quality samples with A260/A230>2.0 and A260/A280>1.8 as determined with a ND-2000 spectrophotometer (Nanodrop Technologies, San Francisco CA, USA) as template for reverse transcription with the M-MLV Reverse Transcriptase kit (Thermo Fisher Scientific). Quantitative real-time PCR reactions were performed using Maxima SYBR® Green Master Mix (Thermo Fisher Scientific) on a CFX384 instrument (Bio-Rad, Hercules, CA, USA). Transcript abundance was normalized to *ACTIN* 2 (AT3G18780). Primers are listed in **Table 7**.

Transgenic lines. An *ACD6* fragment corresponding to Chr4: 8292084..8298360 in the TAIR10 reference genome was amplified from Ty-0 genomic DNA with PCR primers designed based on the *ACD6*-Est-1 sequence. To generate *pACD6::ACD6-3xFLAG* (*ACD6-FLAG*), genomic DNA was amplified from Est-1 and Col-0 plants using an oligonucleotide primer that contained 3xFLAG coding sequence. Fragments were cloned into Gateway entry vector pCR8/GW/TOPO (Thermo Fisher Scientific) and moved into the binary vector pFK206, a modified pGREEN vector with *rbsc* terminator (Hellens et al., 2000) .

For *MHA1, MHA2* and *MHAL* overexpression constructs, coding regions were amplified and cloned into pCR8/GW/TOPO, moved into binary vector pFK210, a modified pGREEN vector with a *35S* CaMV promoter and *rbsc* terminator (Hellens et al., 2000), and introduced into pFAST-G02 (Shimada et al., 2010), which contains a seed coat fluorescence marker. To tag MHA1 and MHAL proteins, mGFP coding sequences were added to *MHA1* and *MHAL* coding sequences using Gibson assembly (NEB, Ipswich, MA, USA). We also generated 2.1 kb genomic constructs for both *MHA1*-Est-1 and *MHA1*-Ty-0 (*pMHA1::MHA1-Est-1* and *pMHA1::MHA1-Ty-0*) with pCR8/GW/TOPO and pFK206. Constructs are listed in **Table 8**.

Mutant screen for *p35S::MHAL* suppressors. 20,000 seeds of a *p35S::MHAL* homozygous line were treated with 0.2% EMS overnight, followed by thorough rinses with water and sowing the seeds on soil. M_2 seeds were collected in 640 pools. In the M_2 generation, we screened for non-necrotic, normal-sized plants. Phenotypic suppression was confirmed in the M_3 generation. Genomic DNA of M_3 plants was extracted, tagmented (Picelli et al., 2014; Rowan et al., 2017), and sequenced on an HiSeq3000 instrument (Illumina)

with 150 bp single-end reads. Raw reads were mapped to the TAIR10 reference genome using BWA-MEM (Li and Durbin, 2009). bcftools (Li et al., 2009) and vcftools (Danecek et al., 2011) were used to call SNPs and generate the final VCF file, followed by snpEff (Cingolani et al., 2012) annotation of SNP effects. Mutations shared by all lines were removed, and genes with at least three independent G>A or C>T mutations predicted to cause non-synonymous changes or truncate the open reading frame were analyzed in detail.

Trypan Blue staining. Freshly harvested leaf tissue was stained by completely immersing it in lacto-phenol/Trypan Blue staining solution (10 mL lactic acid, 10 mL glycerol, 10 mL phenol, 10 mg Trypan Blue and 10 mL water) and heating in a heat block at 80°C for 1 hour. Staining solution was aspirated and replaced by chloral hydrate solution (2.5 g/mL) to destain and clear the tissue. This was repeated once overnight to improve clearing. Samples were kept in 60% (v/v) aqueous glycerol for storage and further imaging.

***Pseudomonas* infection.** *Pst* DC3000 *avrRpt2* was grown to OD_{600} of 3.0 in KB medium, pelleted at 4,000 rpm and resuspended in 10 mM $MgCl_2$ at 5×10^5 colony-forming units (cfu)/ml. The suspension was infiltrated into leaves of 4-week-old *A. thaliana* plants with a needleless syringe. Bacterial growth was determined at 3 days post-inoculation by colony counting (3 dpi). The experiment was repeated twice. The bacterial growth assay of *Pst* DC3000 *hrcC*- followed a published protocol (Tian et al., 2019). In brief, an overnight culture strain was pelleted and resuspended in 10 mM $MgCl_2$ at 1×10^8 cfu/ml in 0.03% Silwet L-77 (Helena, Collierville, TN, USA). Plants were dipped in the bacterial suspension for 30 seconds, and covered with a clear plastic lid. At 4 days post-inoculation, leaf discs were collected and surface sterilized (30 sec in 70% ethanol, followed by 30 sec in sterile distilled water) for colony assays.

Confocal microscopy. Five-day-old *A. thaliana* seedlings were imaged on a TCS SP8 confocal microscope (Leica, Wetzlar, Germany) with a 40x water corrected objective (1.10 NA) and a 488 nm excitation laser at 5% intensity. GFP emission was captured from 499 to 559 nm with a photomultiplier tube, at a gain of 450.3. Propidium Iodide emission was captured from 576 to 691 nm with a Hybrid detector, at a gain of 55.3. For the BFA assay, the laser intensity was reduced to 2%. GFP emission was captured from 507 to 539 nm with a Hybrid detector, at a gain of 10. FM4-64 emission was captured from 705 to 755 nm with a Hybrid detector, at a gain of 50. Images were combined to a frame average of 4.

Subcellular fractionation. We followed a published protocol (El Kasmi et al., 2017) with modification. About 100 mg of 10-day-old *A. thaliana* seedlings were ground on ice with pestle and mortar. 200 µL sucrose buffer (20 mM Tris [pH 8], 0.33 M sucrose, 1 mM EDTA, 1 mM DTT and protease inhibitor cocktail) was added. Samples were spun at 2,000 g for 10 minutes at 4°C to remove plant debris. 45 µL supernatant was removed as total lysate fraction (T). The rest was centrifuged at 20,000 g for 1 hr at 4°C. 45 µL of the resulting supernatant was used as the soluble fraction (S). The membrane pellet was resuspended in 45 µL sucrose buffer and used as microsomal fraction (M).

Split-luciferase complementation assay. We followed a published protocol (Chen et al., 2008). *Agrobacterium tumefaciens* GV3101 with expressions constructs for ACD6-cLuc, MHA1-Est-1-nLuc or MHA1-Ty-0-nLuc were suspended at 5×10^8 cfu/ml in half-strength MS medium. The suspension was

infiltrated into the leaves of 30-day-old *Nicotiana benthamiana* plants. For CCD imaging, leaves were sprayed 48 h later with 1 mM D-Luciferin-K (PJK GmbH, Kleinblittersdorf, Germany) in water containing 0.02% Silwet L-77 (Helena) and kept in the dark for 10 min before measurement. The luminescence signal was recorded with an Orca 2-BT cooled CCD camera (Hamamatsu Photonics, Shizuoka, Japan). The experiment was repeated twice.

Co-immunoprecipitation. ACD6-FLAG was co-expressed with MHA1-GFP and MHAL-GFP in protoplasts isolated from 4-week-old *Arabidopsis thaliana* transgenic plants. Total protein was extracted with extraction buffer (50 mM HEPES [pH 7.5], 150 mM KCl, 1 mM EDTA, 0.5% Triton-X 100, 1 mM DTT, and proteinase inhibitor cocktail). For anti-GFP co-IP, the extracted proteins were incubated with GFP-Trap_M (ChromoTek GmbH, Planegg, Germany) at 4°C under gentle rotation for 2 h. The magnetic particles were washed seven times with washing buffer (50 mM HEPES [pH 7.5], 150 mM KCl, 1 mM EDTA, 0.5% Triton-X 100, 1 mM DTT) at 4°C. Proteins were detected by immunoblotting using anti-GFP (Santa Cruz, California, USA) and anti-FLAG (Sigma-Aldrich, MO, USA) antibodies.

***In vitro* pull-down assays.** GST- and MBP-6xHis-fusion proteins were expressed in *E. coli* BL21. Bacterial cultures in LB were incubated at 28°C until an OD_{600} of 0.6 and then induced with 0.4 mM IPTG at 20°C for 16 hr. Tagged proteins were purified separately using glutathione agarose beads (GE Healthcare, Chicago, USA) or Ni-NTA affinity agarose beads (QIAGEN, Venlo, Netherlands). Purified proteins were dissolved in a buffer containing 25 mM Tris-HCl (pH 7.5), 100 mM NaCl, and 1 mM DTT and concentrated with Amicon Ultra-15 Centrifugal Filter Units (Millipore, Darmstadt, Germany). 2 µg GST-tagged Protein, 20 µl Glutathione Sepharose 4B (GE Healthcare) and 10 µg MBP-6xHis-tagged protein were taken up in 1 ml pull-down buffer (25 mM Tris-HCl [pH 7.5], 200 mM NaCl, 0.5% [v/v] Triton X-100) and incubated for 4 hr under gentle rotation. For washing, the beads with bound protein were spun down (500 rpm, 10 min), the supernatant was discarded, beads were resuspended in pull-down buffer and incubated for 1 hr under gentle rotation. Washing was repeated 6 times. Elution of GST-tagged protein from beads was performed by resuspending pelleted beads (500 rpm, 10 min) in 100 µl Elution buffer (25 mM Tris-HCl [pH 7.5], 150 mM NaCl, 30 mM glutathione) and incubated for 1 hr under gentle rotation. After centrifugation (1,000 rpm, 20 min), GST-tagged protein eluate was collected from supernatant. Protein purification and pull-down were performed at 4°C. Proteins were detected by immunoblotting using anti-Glutathione-S-Transferase (Sigma-Aldrich, MO, USA) and antipolyHistidine-Peroxidase (Sigma-Aldrich, MO, USA) antibodies.

Blue Native-PAGE. Blue native polyacrylamide gel electrophoresis (BN-PAGE) was performed using the Bis-Tris NativePAGE system from Invitrogen (Carlsbad, CA, USA) according to the manufacturer's instructions. Briefly, eight 10-day-old seedlings were collected and ground in 1×NativePAGE Sample Buffer (Invitrogen) containing 1% n-dodecyl β-D-maltoside (DDM) and protease inhibitor cocktail, followed by 13,000 rpm centrifugation for 20 min at 4°C. 20 µL supernatant mixed with 1 µL 5% G-250 Sample Additive was loaded and run on a NativePAGE 3-12% Bis-Tris gel. Native gels were transferred to PVDF membranes (Millipore, Darmstadt, Germany) using NuPAGE Transfer Buffer, followed by protein blotting. For the second

dimension of electrophoresis, a 5.7 cm strip of BN-PAGE gel was incubated in Laemmli sample buffer (50 mM Tris-HCl [pH 6.8], 100 mM DTT, 2% (w/v) SDS, 0.1% bromophenol blue, 10% (v/v) glycerol) for 10 min, microwaved for 20 sec, and then rotated for another 5 min before loading the strip into the well of a NuPAGE 4-12% Bis-Tris protein gel (Invitrogen).

Protein homology search and alignment. HHPred search and structure modeling with MODELLER were performed online (https://toolkit.tuebingen.mpg.de/#/tools/hhpred), using the MPI Bioinformatics Toolkit (Zimmermann et al., 2018). HHPred default search parameter was used for homology searches with ACD6-Col-0 (excluding residues 1-90) as query. Alignments were visualized with Jalview (Waterhouse et al., 2009) Default parameters were used for homology modeling with MODELLER (Sali and Blundell, 1993). We used the SMART database (http://smart.embl-heidelberg.de/) to predict the boundaries of the ankyrin repeats in ACD6, and the TMHMM server v2.0 (http://www.cbs.dtu.dk/services/TMHMM/) to predict transmembrane domains. Structures were visualized using PyMOL (Schrödinger LLC, 2010).

Injection of oocytes and electrophysiological measurements. Dissected and preselected *Xenopus laevis* oocytes were obtained from Ecocyte Bioscience (Dortmund, Germany). Oocytes were kept in ND96 (96 mM NaCl, 2 mM KCl, 1 mM $MgCl_2$, 1.8 mM $CaCl_2$, 2.5 mM sodium pyruvate, 5 mM HEPES adjusted to pH of 7.4 with NaOH). cRNA was produced from *MluI* linearized and phenol-chloroform purified pOO2 plasmids (Straub et al., 2017) containing the coding sequences of ACD6-1, ACD6-Col-0 or MHAL using the mMESSAGE mMACHINE™ SP6 Transcription Kit (Life Technologies GmbH, Darmstadt; Germany) following the manufacturer's instructions. Oocytes were injected with 50 nl cRNA with a concentration of 300 ng/µl for ACD6 variants and 0.1 ng/µl for MHAL. Oocytes were kept in ND96 for 3-4 days at 18 °C. Electrophysiology was performed in a small recording chamber containing the recording solution.

For sodium transport measurements the test solution contained 110 mM choline chloride, 2 mM $CaCl_2$, 2 mM $MgCl_2$, 5 mM N-morpholinoethane sulfonate (MES), pH adjusted to 5.5 with Tris(hydroxymethyl) aminomethane (TRIS) with and without 10 mM NaCl. Recording solutions for calcium-induced chloride currents were: -Cl solution (100 mM sodium glutamate, 5 mM MES, pH adjusted to 5.5 with TRIS); -Cl/+Ca solution (90 mM sodium glutamate, 10 mM $CaNO_3$, 5 mM MES, pH adjusted to 5.5 with TRIS); -Ca solution (100 mM sodium chloride, 5 mM MES, pH adjusted to 5.5 with TRIS) and +Ca solution (90 mM sodium chloride, 10 mM $CaCl_2$, 5 mM MES, pH adjusted to 5.5 with TRIS).

Two-electrode voltage-clamp measurements were performed using 3 M KCl-filled glass capillaries of around 2 Mohm resistance of the electrodes. For measurements in -Cl solutions, an agarose bridge was used to connect the recording chamber with a separated reference electrode bathed in 3 M KCl solution via a glass capillary filled with 3 M KCl and 2 % agarose. Currents were recorded with 100 ms steps over a range from +80 mV to -140 mV in 10 or 20 mV decrements. Electrical recordings were performed after complete wash of the bathing solutions to test solutions and the mean induced currents by the test solutions are shown (background currents were subtracted). Data from representative oocyte batches are shown.

URLs. *Arabidopsis thaliana* 1001 Genomes Project http://1001genomes.org; Univ. of Toronto gene expression browser http://bar.utoronto.ca; easyGWAS https://easygwas.ethz.ch; HHPred toolkit.tuebingen.mpg.de.

Accession codes. Sanger sequences are available at Genbank: *ACD6*-Ty-0 MH120293, *MHA1*-Ty-0 MH120291, *MHA1*-Est-1 MH120292, *MHA2*-Est-1 MK977584, and *MHA2*-Ty-0 MK977584.

Acknowledgements

We thank past and present members of the Weigel lab, Richard Hilleary and Sheng Yang He, Katherine Huffer and Kenton Swartz, and Yalong Guo for discussion, and Farid El-Kasmi, Derek Lundberg, Wei Yuan, Alejandra Duque and Thorsten Nürnberger for comments on the manuscript. We thank Maricris Zaidem for seeds of the Ty-0 x Est-1 F_2 population and Polina Novikova for resequencing data of natural *Arabidopsis lyrata* accessions. We thank Monika Demar, Frederik Unger, Sonja Kersten, Kai Wang, and Martin Bayer for help with experiments, and the ZMBP Analytics Laboratory from the University of Tübingen for help with salicylic acid quantification. This work was supported by an EMBO Long-term Fellowship (969-2016 to L.L.), an HFSP Long-term Fellowship (LT000314/2017-L to L.L.), the DFG (NE 1727/2-2 to B.N.), a Starting Grant from China Agricultural University (W.Z.), the Ministry of Science Research and Arts Baden-Württemberg through the Regio Research Alliance "Yield Stability in Dynamic Environments" (U.L., D.W.), the DFG through SFB1101, and the Max Planck Society (D.W.).

Author Contributions

Conceptualization: W.Z., L.L., U.Lud., D.W. Methodology: W.Z., L.L., B.N. Formal analysis: W.Z. Investigation: W.Z., L.L., B.N., M.T., M.W., J.C., L.W., K.V., M.E.A., C.L., J.K., A.C.B, R.S., U.Lut.. Writing–original draft: W.Z., D.W.. Writing–review, and editing: W.Z., L.L., U.Lud., D.W. Supervision: W.Z., U.Lud., D.W. Project administration: D.W. Funding acquisition: W.Z., L.L., U.Lud., D.W.

Completing Financial Interests

The authors declare no competing interests.

References

1001 Genomes Consortium. 2016. 1,135 Genomes Reveal the Global Pattern of Polymorphism in Arabidopsis thaliana. *Cell* **166**:481–491.

Arbabian A, Iftinca M, Altier C, Singh PP, Isambert H, Coscoy S. 2020. Mutations in calmodulin-binding domains of TRPV4/6 channels confer invasive properties to colon adenocarcinoma cells. *Channels* **14**:101–109.

Arif Pavel M, Lv C, Ng C, Yang L, Kashyap P, Lam C, Valentino V, Fung HY, Campbell T, Møller SG, Zenisek D, Holtzman NG, Yu Y. 2016. Function and regulation of TRPP2 ion channel revealed by a gain-of-function mutant. *Proc Natl Acad Sci U S A* **113**:E2363–72.

Becerra C, Jahrmann T, Puigdomènech P, Vicient CM. 2004. Ankyrin repeat-containing proteins in

Arabidopsis: characterization of a novel and abundant group of genes coding ankyrin-transmembrane proteins. *Gene* **340**:111–121.

Bonardi V, Tang S, Stallmann A, Roberts M, Cherkis K, Dangl JL. 2011. Expanded functions for a family of plant intracellular immune receptors beyond specific recognition of pathogen effectors. *Proc Natl Acad Sci U S A* **108**:16463–16468.

Boukalova S, Marsakova L, Teisinger J, Vlachova V. 2010. Conserved residues within the putative S4-S5 region serve distinct functions among thermosensitive vanilloid transient receptor potential (TRPV) channels. *J Biol Chem* **285**:41455–41462.

Bredow M, Monaghan J. 2019. Regulation of Plant Immune Signaling by Calcium-Dependent Protein Kinases. *Mol Plant Microbe Interact* **32**:6–19.

Broman KW, Wu H, Sen S, Churchill GA. 2003. R/qtl: QTL mapping in experimental crosses. *Bioinformatics* **19**:889–890.

Castel B, Ngou P-M, Cevik V, Redkar A, Kim D-S, Yang Y, Ding P, Jones JDG. 2019. Diverse NLR immune receptors activate defence via the RPW8-NLR NRG1. *New Phytol* **222**:966–980.

Cheng N-H, Pittman JK, Shigaki T, Lachmansingh J, LeClere S, Lahner B, Salt DE, Hirschi KD. 2005. Functional association of Arabidopsis CAX1 and CAX3 is required for normal growth and ion homeostasis. *Plant Physiol* **138**:2048–2060.

Chen H, Zou Y, Shang Y, Lin H, Wang Y, Cai R, Tang X, Zhou J-M. 2008. Firefly luciferase complementation imaging assay for protein-protein interactions in plants. *Plant Physiol* **146**:368–376.

Cingolani P, Platts A, Wang LL, Coon M, Nguyen T, Wang L, Land SJ, Lu X, Ruden DM. 2012. A program for annotating and predicting the effects of single nucleotide polymorphisms, SnpEff: SNPs in the genome of Drosophila melanogaster strain w1118; iso-2; iso-3. *Fly* **6**:80–92.

Clough SJ, Fengler KA, Yu IC, Lippok B, Smith RK Jr, Bent AF. 2000. The Arabidopsis dnd1 "defense, no death" gene encodes a mutated cyclic nucleotide-gated ion channel. *Proc Natl Acad Sci U S A* **97**:9323–9328.

Contento AL, Bassham DC. 2012. Structure and function of endosomes in plant cells. *J Cell Sci* **125**:3511–3518.

Cui H, Gobbato E, Kracher B, Qiu J, Bautor J, Parker JE. 2017. A core function of EDS1 with PAD4 is to protect the salicylic acid defense sector in Arabidopsis immunity. *New Phytol* **213**:1802–1817.

Danecek P, Auton A, Abecasis G, Albers CA, Banks E, DePristo MA, Handsaker RE, Lunter G, Marth GT, Sherry ST, McVean G, Durbin R, 1000 Genomes Project Analysis Group. 2011. The variant call format and VCFtools. *Bioinformatics* **27**:2156–2158.

Dong X-P, Wang X, Shen D, Chen S, Liu M, Wang Y, Mills E, Cheng X, Delling M, Xu H. 2009. Activating mutations of the TRPML1 channel revealed by proline-scanning mutagenesis. *J Biol Chem* **284**:32040–32052.

Eichler EE, Flint J, Gibson G, Kong A, Leal SM, Moore JH, Nadeau JH. 2010. Missing heritability and strategies for finding the underlying causes of complex disease. *Nat Rev Genet* **11**:446–450.

El Kasmi F, Chung E-H, Anderson RG, Li J, Wan L, Eitas TK, Gao Z, Dangl JL. 2017. Signaling from the plasma-membrane localized plant immune receptor RPM1 requires self-association of the full-length protein. *Proc Natl Acad Sci U S A*. doi:10.1073/pnas.1708288114

Fu ZQ, Dong X. 2013. Systemic acquired resistance: turning local infection into global defense. *Annu Rev Plant Biol* **64**:839–863.

Gaffney T, Friedrich L, Vernooij B, Negrotto D, Nye G, Uknes S, Ward E, Kessmann H, Ryals J. 1993. Requirement of salicylic Acid for the induction of systemic acquired resistance. *Science* **261**:754–756.

Gao X, Chen J, Dai X, Zhang D, Zhao Y. 2016. An Effective Strategy for Reliably Isolating Heritable and Cas9-Free Arabidopsis Mutants Generated by CRISPR/Cas9-Mediated Genome Editing. *Plant Physiol* **171**:1794–1800.

Gazzani S, Lawrenson T, Woodward C, Headon D, Sablowski R. 2004. A link between mRNA turnover and RNA interference in Arabidopsis. *Science* **306**:1046–1048.

Gibson G, Dworkin I. 2004. Uncovering cryptic genetic variation. *Nat Rev Genet* **5**:681–690.

Grant M, Brown I, Adams S, Knight M, Ainslie A, Mansfield J. 2000. The RPM1 plant disease resistance gene facilitates a rapid and sustained increase in cytosolic calcium that is necessary for the oxidative burst and hypersensitive cell death. *Plant J* **23**:441–450.

Grimm C, Cuajungco MP, van Aken AFJ, Schnee M, Jörs S, Kros CJ, Ricci AJ, Heller S. 2007. A helix-breaking mutation in TRPML3 leads to constitutive activity underlying deafness in the varitint-waddler mouse. *Proc Natl Acad Sci U S A* **104**:19583–19588.

Grimm DG, Roqueiro D, Salome P, Kleeberger S, Greshake B, Zhu W, Liu C, Lippert C, Stegle O, Schölkopf

B, Weigel D, Borgwardt K. 2016. easyGWAS: A Cloud-based Platform for Comparing the Results of Genome-wide Association Studies. *Plant Cell*. doi:10.1105/tpc.16.00551

Hartzell C, Putzier I, Arreola J. 2005. Calcium-activated chloride channels. *Annu Rev Physiol* **67**:719–758.

Hellens RP, Edwards EA, Leyland NR, Bean S, Mullineaux PM. 2000. pGreen: a versatile and flexible binary Ti vector for Agrobacterium-mediated plant transformation. *Plant Mol Biol* **42**:819–832.

Hilleary R, Paez-Valencia J, Vens C, Toyota M, Palmgren M, Gilroy S. 2020. Tonoplast-localized Ca2+ pumps regulate Ca2+ signals during pattern-triggered immunity in Arabidopsis thaliana. *Proc Natl Acad Sci U S A*. doi:10.1073/pnas.2004183117

Hong YS, Park S, Geng C, Baek K, Bowman JD, Yoon J, Pak WL. 2002. Single amino acid change in the fifth transmembrane segment of the TRP Ca2+ channel causes massive degeneration of photoreceptors. *J Biol Chem* **277**:33884–33889.

Huffer KE, Aleksandrova AA, Jara-Oseguera A, Forrest LR, Swartz KJ. 2020. Global alignment and assessment of TRP channel transmembrane domain structures to explore functional mechanisms. *Elife* **9**. doi:10.7554/eLife.58660

Hurni S, Brunner S, Stirnweis D, Herren G, Peditto D, McIntosh RA, Keller B. 2014. The powdery mildew resistance gene Pm8 derived from rye is suppressed by its wheat ortholog Pm3. *Plant J* **79**:904–913.

Julius D. 2013. TRP channels and pain. *Annu Rev Cell Dev Biol* **29**:355–384.

Jung C, Gené GG, Tomás M, Plata C, Selent J, Pastor M, Fandos C, Senti M, Lucas G, Elosua R, Valverde MA. 2011. A gain-of-function SNP in TRPC4 cation channel protects against myocardial infarction. *Cardiovasc Res* **91**:465–471.

Kim HJ, Li Q, Tjon-Kon-Sang S, So I, Kiselyov K, Muallem S. 2007. Gain-of-function mutation in TRPML3 causes the mouse Varitint-Waddler phenotype. *J Biol Chem* **282**:36138–36142.

Kover PX, Caicedo AL. 2001. The genetic architecture of disease resistance in plants and the maintenance of recombination by parasites. *Mol Ecol* **10**:1–16.

Kremeyer B, Lopera F, Cox JJ, Momin A, Rugiero F, Marsh S, Woods CG, Jones NG, Paterson KJ, Fricker FR, Villegas A, Acosta N, Pineda-Trujillo NG, Ramírez JD, Zea J, Burley M-W, Bedoya G, Bennett DLH, Wood JN, Ruiz-Linares A. 2010. A gain-of-function mutation in TRPA1 causes familial episodic pain syndrome. *Neuron* **66**:671–680.

Krogh A, Larsson B, von Heijne G, Sonnhammer EL. 2001. Predicting transmembrane protein topology with a hidden Markov model: application to complete genomes. *J Mol Biol* **305**:567–580.

Lampropoulos A, Sutikovic Z, Wenzl C, Maegele I, Lohmann JU, Forner J. 2013. GreenGate - A Novel, Versatile, and Efficient Cloning System for Plant Transgenesis. *PLoS One* **8**:e83043.

Landouré G, Zdebik AA, Martinez TL, Burnett BG, Stanescu HC, Inada H, Shi Y, Taye AA, Kong L, Munns CH, Choo SS, Phelps CB, Paudel R, Houlden H, Ludlow CL, Caterina MJ, Gaudet R, Kleta R, Fischbeck KH, Sumner CJ. 2010. Mutations in TRPV4 cause Charcot-Marie-Tooth disease type 2C. *Nat Genet* **42**:170–174.

Lange H, Ndecky SYA, Gomez-Diaz C, Pflieger D, Butel N, Zumsteg J, Kuhn L, Piermaria C, Chicher J, Christie M, Karaaslan ES, Lang PLM, Weigel D, Vaucheret H, Hammann P, Gagliardi D. 2019. RST1 and RIPR connect the cytosolic RNA exosome to the Ski complex in Arabidopsis. *Nat Commun* **10**:3871.

Lapin D, Bhandari DD, Parker JE. 2020. Origins and Immunity Networking Functions of EDS1 Family Proteins. *Annu Rev Phytopathol*. doi:10.1146/annurev-phyto-010820-012840

Li H, Durbin R. 2009. Fast and accurate short read alignment with Burrows-Wheeler transform. *Bioinformatics* **25**:1754–1760.

Li H, Handsaker B, Wysoker A, Fennell T, Ruan J, Homer N, Marth G, Abecasis G, Durbin R, 1000 Genome Project Data Processing Subgroup. 2009. The Sequence Alignment/Map format and SAMtools. *Bioinformatics* **25**:2078–2079.

Li J-F, Norville JE, Aach J, McCormack M, Zhang D, Bush J, Church GM, Sheen J. 2013. Multiplex and homologous recombination–mediated genome editing in Arabidopsis and Nicotiana benthamiana using guide RNA and Cas9. *Nat Biotechnol* **31**:688.

Li L, Habring A, Wang K, Weigel D. 2020. Atypical Resistance Protein RPW8/HR Triggers Oligomerization of the NLR Immune Receptor RPP7 and Autoimmunity. *Cell Host Microbe*. doi:10.1016/j.chom.2020.01.012

Lin Z, Chen Q, Lee M, Cao X, Zhang J, Ma D, Chen L, Hu X, Wang H, Wang X, Zhang P, Liu X, Guan L, Tang Y, Yang H, Tu P, Bu D, Zhu X, Wang K, Li R, Yang Y. 2012. Exome sequencing reveals mutations in TRPV3 as a cause of Olmsted syndrome. *Am J Hum Genet* **90**:558–564.

Lishko PV, Procko E, Jin X, Phelps CB, Gaudet R. 2007. The ankyrin repeats of TRPV1 bind multiple ligands and modulate channel sensitivity. *Neuron* **54**:905–918.

Li T, Natran A, Chen Y, Vercruysse J, Wang K, Gonzalez N, Dubois M, Inzé D. 2019. A genetics screen highlights emerging roles for CPL3, RST1 and URT1 in RNA metabolism and silencing. *Nat Plants* **5**:539–550.

Liu H, El Zein L, Kruse M, Guinamard R, Beckmann A, Bozio A, Kurtbay G, Mégarbané A, Ohmert I, Blaysat G, Villain E, Pongs O, Bouvagnet P. 2010. Gain-of-function mutations in TRPM4 cause autosomal dominant isolated cardiac conduction disease. *Circ Cardiovasc Genet* **3**:374–385.

Loudet O, Gaudon V, Trubuil A, Daniel-Vedele F. 2005. Quantitative trait loci controlling root growth and architecture in Arabidopsis thaliana confirmed by heterogeneous inbred family. *Theor Appl Genet* **110**:742–753.

Lu H, Greenberg JT, Holuigue L. 2016. Editorial: Salicylic Acid Signaling Networks. *Front Plant Sci* **7**:238.

Lu H, Liu Y, Greenberg JT. 2005. Structure-function analysis of the plasma membrane- localized Arabidopsis defense component ACD6. *Plant J* **44**:798–809.

Lu H, Rate DN, Song JT, Greenberg JT. 2003. ACD6, a novel ankyrin protein, is a regulator and an effector of salicylic acid signaling in the Arabidopsis defense response. *Plant Cell* **15**:2408–2420.

Mackay TFC. 2014. Epistasis and quantitative traits: using model organisms to study gene-gene interactions. *Nat Rev Genet* **15**:22–33.

Mah W, Sonkusare SK, Wang T, Azeddine B, Pupavac M, Carrot-Zhang J, Hong K, Majewski J, Harvey EJ, Russell L, Chalk C, Rosenblatt DS, Nelson MT, Séguin C. 2016. Gain-of-function mutation in TRPV4 identified in patients with osteonecrosis of the femoral head. *J Med Genet* **53**:705–709.

Manolio TA, Collins FS, Cox NJ, Goldstein DB, Hindorff LA, Hunter DJ, McCarthy MI, Ramos EM, Cardon LR, Chakravarti A, Cho JH, Guttmacher AE, Kong A, Kruglyak L, Mardis E, Rotimi CN, Slatkin M, Valle D, Whittemore AS, Boehnke M, Clark AG, Eichler EE, Gibson G, Haines JL, Mackay TF, McCarroll SA, Visscher PM. 2009. Finding the missing heritability of complex diseases. *Nature* **461**:747–753.

Ma W, Berkowitz GA. 2007. The grateful dead: calcium and cell death in plant innate immunity. *Cell Microbiol* **9**:2571–2585.

Moeder W, Phan V, Yoshioka K. 2019. Ca2+ to the rescue - Ca2+channels and signaling in plant immunity. *Plant Sci* **279**:19–26.

Myers BR, Bohlen CJ, Julius D. 2008a. A yeast genetic screen reveals a critical role for the pore helix domain in TRP channel gating. *Neuron* **58**:362–373.

Myers BR, Saimi Y, Julius D, Kung C. 2008b. Multiple unbiased prospective screens identify TRP channels and their conserved gating elements. *J Gen Physiol* **132**:481–486.

Nagata K, Zheng L, Madathany T, Castiglioni AJ, Bartles JR, García-Añoveros J. 2008. The varitint-waddler (Va) deafness mutation in TRPML3 generates constitutive, inward rectifying currents and causes cell degeneration. *Proc Natl Acad Sci U S A* **105**:353–358.

Ng G, Seabolt S, Zhang C, Salimian S, Watkins TA, Lu H. 2011. Genetic dissection of salicylic acid-mediated defense signaling networks in Arabidopsis. *Genetics* **189**:851–859.

Paaby AB, Rockman MV. 2014. Cryptic genetic variation: evolution's hidden substrate. *Nat Rev Genet* **15**:247–258.

Paulus JK, Kourelis J, Ramasubramanian S, Homma F, Godson A, Hörger AC, Hong TN, Krahn D, Ossorio Carballo L, Wang S, Win J, Smoker M, Kamoun S, Dong S, van der Hoorn RAL. 2020. Extracellular proteolytic cascade in tomato activates immune protease Rcr3. *Proc Natl Acad Sci U S A* **117**:17409–17417.

Picelli S, Björklund AK, Reinius B, Sagasser S, Winberg G, Sandberg R. 2014. Tn5 transposase and tagmentation procedures for massively scaled sequencing projects. *Genome Res* **24**:2033–2040.

Pruitt RN, Zhang L, Saile SC, Karelina D, Fröhlich K, Wan W-L, Rao S, Gust AA, Locci F, Matthieu H A, Bart P H, Zhou J-M, Dangl JL, Weigel D, Parker JE, El Kasmi F, Nürnberger T. 2020. Arabidopsis cell surface LRR immune receptor signaling through the EDS1-PAD4-ADR1 node. *bioRxiv*. doi:10.1101/2020.11.23.391516

Qi Z, Verma R, Gehring C, Yamaguchi Y, Zhao Y, Ryan CA, Berkowitz GA. 2010. Ca2+ signaling by plant Arabidopsis thaliana Pep peptides depends on AtPepR1, a receptor with guanylyl cyclase activity, and cGMP-activated Ca2+ channels. *Proc Natl Acad Sci U S A* **107**:21193–21198.

Ramírez V, López A, Mauch-Mani B, Gil MJ, Vera P. 2013. An extracellular subtilase switch for immune priming in Arabidopsis. *PLoS Pathog* **9**:e1003445.

Rate DN, Cuenca JV, Bowman GR, Guttman DS, Greenberg JT. 1999. The gain-of-function Arabidopsis acd6 mutant reveals novel regulation and function of the salicylic acid signaling pathway in controlling cell death, defenses, and cell growth. *Plant Cell* **11**:1695–1708.

R Core Team. 2019. R: A Language and Environment for Statistical Computing.

Reichardt S, Repper D, Tuzhikov AI, Galiullina RA, Planas-Marquès M, Chichkova NV, Vartapetian AB, Stintzi A, Schaller A. 2018. The tomato subtilase family includes several cell death-related proteinases with caspase specificity. *Sci Rep* **8**:10531.

Reiser J, Polu KR, Möller CC, Kenlan P, Altintas MM, Wei C, Faul C, Herbert S, Villegas I, Avila-Casado C, McGee M, Sugimoto H, Brown D, Kalluri R, Mundel P, Smith PL, Clapham DE, Pollak MR. 2005. TRPC6 is a glomerular slit diaphragm-associated channel required for normal renal function. *Nat Genet* **37**:739–744.

Rowan BA, Seymour DK, Chae E, Lundberg DS, Weigel D. 2017. Methods for Genotyping-by-Sequencing. *Methods Mol Biol* **1492**:221–242.

Sali A, Blundell TL. 1993. Comparative protein modelling by satisfaction of spatial restraints. *J Mol Biol* **234**:779–815.

Schaller A, Stintzi A, Rivas S, Serrano I, Chichkova NV, Vartapetian AB, Martínez D, Guiamét JJ, Sueldo DJ, van der Hoorn RAL, Ramírez V, Vera P. 2018. From structure to function - a family portrait of plant subtilases. *New Phytol* **218**:901–915.

Schrödinger LLC. 2010. The PyMOL Molecular Graphics System, Version 1.3r1.

Seybold H, Trempel F, Ranf S, Scheel D, Romeis T, Lee J. 2014. Ca2+ signalling in plant immune response: from pattern recognition receptors to Ca2+ decoding mechanisms. *New Phytol* **204**:782–790.

Seyfferth C, Tsuda K. 2014. Salicylic acid signal transduction: the initiation of biosynthesis, perception and transcriptional reprogramming. *Front Plant Sci* **5**:697.

Shimada TL, Shimada T, Hara-Nishimura I. 2010. A rapid and non-destructive screenable marker, FAST, for identifying transformed seeds of Arabidopsis thaliana. *Plant J* **61**:519–528.

Soltis NE, Kliebenstein DJ. 2015. Natural Variation of Plant Metabolism: Genetic Mechanisms, Interpretive Caveats, and Evolutionary and Mechanistic Insights. *Plant Physiol* **169**:1456–1468.

Stirnweis D, Milani SD, Brunner S, Herren G, Buchmann G, Peditto D, Jordan T, Keller B. 2014. Suppression among alleles encoding nucleotide-binding-leucine-rich repeat resistance proteins interferes with resistance in F1 hybrid and allele-pyramided wheat plants. *Plant J* **79**:893–903.

Straub T, Ludewig U, Neuhäuser B. 2017. The Kinase CIPK23 Inhibits Ammonium Transport in Arabidopsis thaliana. *Plant Cell* **29**:409–422.

Sun X, Lapin D, Feehan JM, Stolze SC, Kramer K, Dongus JA, Rzemieniewski J, Blanvillain-Baufumé S, Harzen A, Bautor J, Derbyshire P, Menke FLH, Finkemeier I, Nakagami H, Jones JDG, Parker JE. 2020. Pathogen effector recognition-dependent association of NRG1 with EDS1 and SAG101 in TNL receptor immunity. *bioRxiv*. doi:10.1101/2020.12.21.423810

Su Z, Zhou X, Haynes WJ, Loukin SH, Anishkin A, Saimi Y, Kung C. 2007. Yeast gain-of-function mutations reveal structure-function relationships conserved among different subfamilies of transient receptor potential channels. *Proc Natl Acad Sci U S A* **104**:19607–19612.

Świadek M, Proost S, Sieh D, Yu J, Todesco M, Jorzig C, Rodriguez Cubillos AE, Plötner B, Nikoloski Z, Chae E, Giavalisco P, Fischer A, Schröder F, Kim S-T, Weigel D, Laitinen RAE. 2016. Novel allelic variants in ACD6 cause hybrid necrosis in local collection of Arabidopsis thaliana. *New Phytol*. doi:10.1111/nph.14155

Tamura K, Stecher G, Peterson D, Filipski A, Kumar S. 2013. MEGA6: Molecular Evolutionary Genetics Analysis version 6.0. *Mol Biol Evol* **30**:2725–2729.

Tateda C, Zhang Z, Shrestha J, Jelenska J, Chinchilla D, Greenberg JT. 2014. Salicylic acid regulates Arabidopsis microbial pattern receptor kinase levels and signaling. *Plant Cell* **26**:4171–4187.

Thor K, Jiang S, Michard E, George J, Scherzer S, Huang S, Dindas J, Derbyshire P, Leitão N, DeFalco TA, Köster P, Hunter K, Kimura S, Gronnier J, Stransfeld L, Kadota Y, Bücherl CA, Charpentier M, Wrzaczek M, MacLean D, Oldroyd GED, Menke FLH, Roelfsema MRG, Hedrich R, Feijó J, Zipfel C. 2020. The calcium-permeable channel OSCA1.3 regulates plant stomatal immunity. *Nature*. doi:10.1038/s41586-020-2702-1

Tian W, Hou C, Ren Z, Wang C, Zhao F, Dahlbeck D, Hu S, Zhang L, Niu Q, Li L, Staskawicz BJ, Luan S. 2019. A calmodulin-gated calcium channel links pathogen patterns to plant immunity. *Nature*. doi:10.1038/s41586-019-1413-y

Todesco M, Balasubramanian S, Hu TT, Traw MB, Horton M, Epple P, Kuhns C, Sureshkumar S, Schwartz C, Lanz C, Laitinen RAE, Huang Y, Chory J, Lipka V, Borevitz JO, Dangl JL, Bergelson J, Nordborg M, Weigel D. 2010. Natural allelic variation underlying a major fitness trade-off in Arabidopsis thaliana. *Nature* **465**:632–636.

Todesco M, Kim S-T, Chae E, Bomblies K, Zaidem M, Smith LM, Weigel D, Laitinen RAE. 2014. Activation of the Arabidopsis thaliana Immune System by Combinations of Common ACD6 Alleles. *PLoS Genet*

10:e1004459.

Tran DTN, Chung E-H, Habring-Müller A, Demar M, Schwab R, Dangl JL, Weigel D, Chae E. 2017. Activation of a Plant NLR Complex through Heteromeric Association with an Autoimmune Risk Variant of Another NLR. *Curr Biol* **27**:1148–1160.

Van Hoeymissen E, Held K, Nogueira Freitas AC, Janssens A, Voets T, Vriens J. 2020. Gain of channel function and modified gating properties in TRPM3 mutants causing intellectual disability and epilepsy. *Elife* **9**. doi:10.7554/eLife.57190

van Wersch R, Li X, Zhang Y. 2016. Mighty Dwarfs: Arabidopsis Autoimmune Mutants and Their Usages in Genetic Dissection of Plant Immunity. *Front Plant Sci* **7**:1717.

Vasseur F, Fouqueau L, de Vienne D, Nidelet T, Violle C, Weigel D. 2019. Nonlinear phenotypic variation uncovers the emergence of heterosis in Arabidopsis thaliana. *PLoS Biol* **17**:e3000214.

Venkatachalam K, Montell C. 2007. TRP channels. *Annu Rev Biochem* **76**:387–417.

Vlot AC, Dempsey DA, Klessig DF. 2009. Salicylic Acid, a multifaceted hormone to combat disease. *Annu Rev Phytopathol* **47**:177–206.

Vo KTX, Kimauthor C-Y, Chandranauthor AKN, Jungauthor K-H, Anauthor G, Jeonauthor J-S. 2015. Molecular insights into the function of ankyrin proteins in plants. doi:10.1007/s12374-015-0228-0

Wang G, Wang K. 2017. The Ca2+-Permeable Cation Transient Receptor Potential TRPV3 Channel: An Emerging Pivotal Target for Itch and Skin Diseases. *Mol Pharmacol* **92**:193–200.

Wang H, Xu Z, Lee BH, Vu S, Hu L, Lee M, Bu D, Cao X, Hwang S, Yang Y, Zheng J, Lin Z. 2019. Gain-of-Function Mutations in TRPM4 Activation Gate Cause Progressive Symmetric Erythrokeratodermia. *J Invest Dermatol* **139**:1089–1097.

Wang J, Hu M, Wang J, Qi J, Han Z, Wang G, Qi Y, Wang H-W, Zhou J-M, Chai J. 2019. Reconstitution and structure of a plant NLR resistosome conferring immunity. *Science* **364**:eaav5870.

Waterhouse AM, Procter JB, Martin DMA, Clamp M, Barton GJ. 2009. Jalview Version 2--a multiple sequence alignment editor and analysis workbench. *Bioinformatics* **25**:1189–1191.

Winn MP, Conlon PJ, Lynn KL, Farrington MK, Creazzo T, Hawkins AF, Daskalakis N, Kwan SY, Ebersviller S, Burchette JL, Pericak-Vance MA, Howell DN, Vance JM, Rosenberg PB. 2005. A mutation in the TRPC6 cation channel causes familial focal segmental glomerulosclerosis. *Science* **308**:1801–1804.

Winter D, Vinegar B, Nahal H, Ammar R, Wilson GV, Provart NJ. 2007. An "Electronic Fluorescent Pictograph" browser for exploring and analyzing large-scale biological data sets. *PLoS One* **2**:e718.

Wróblewski T, Spiridon L, Martin EC, Petrescu A-J, Cavanaugh K, Jose-Truco M, Xu H, Gozdowski D, Pawłowski K, Michelmore RW, Takken FLW. 2018. Genome-wide functional analyses of plant coiled-coil NLR-type pathogen receptors reveal essential roles of their N-terminal domain in oligomerization, networking, and immunity. *PLoS Biol* **16**:e2005821.

Wu C-H, Abd-El-Haliem A, Bozkurt TO, Belhaj K, Terauchi R, Vossen JH, Kamoun S. 2017. NLR network mediates immunity to diverse plant pathogens. *Proc Natl Acad Sci U S A* **114**:8113–8118.

Wu R, Lucke M, Jang Y-T, Zhu W, Symeonidi E, Wang C, Fitz J, Xi W, Schwab R, Weigel D. 2018. An efficient CRISPR vector toolbox for engineering large deletions in Arabidopsis thaliana. *Plant Methods* **14**:65.

Wu Z, Li M, Dong OX, Xia S, Liang W, Bao Y, Wasteneys G, Li X. 2019. Differential regulation of TNL-mediated immune signaling by redundant helper CNLs. *New Phytol* **222**:938–953.

Xu H, Delling M, Li L, Dong X, Clapham DE. 2007. Activating mutation in a mucolipin transient receptor potential channel leads to melanocyte loss in varitint-waddler mice. *Proc Natl Acad Sci U S A* **104**:18321–18326.

Yang Y, Zhang Y, Ding P, Johnson K, Li X, Zhang Y. 2012. The ankyrin-repeat transmembrane protein BDA1 functions downstream of the receptor-like protein SNC2 to regulate plant immunity. *Plant Physiol* **159**:1857–1865.

Zhang Z, Guo J, Zhao Y, Chen J. 2019. Identification and characterization of maize ACD6-like gene reveal ZmACD6 as the maize orthologue conferring resistance to Ustilago maydis. *Plant Signal Behav* **14**:e1651604.

Zhang Z, Shrestha J, Tateda C, Greenberg JT. 2014. Salicylic acid signaling controls the maturation and localization of the arabidopsis defense protein ACCELERATED CELL DEATH6. *Mol Plant* **7**:1365–1383.

Zhang Z, Tateda C, Jiang S-C, Shrestha J, Jelenska J, Speed DJ, Greenberg J. 2017. A suite of receptor-like kinases and a putative mechano-sensitive channel are involved in autoimmunity and plasma membrane-based defenses in Arabidopsis. *Mol Plant Microbe Interact*. doi:10.1094/MPMI-09-16-0184-R

Zhu W, Zaidem M, Van de Weyer A-L, Gutaker RM, Chae E, Kim S-T, Bemm F, Li L, Todesco M, Schwab R, Unger F, Beha MJ, Demar M, Weigel D. 2018. Modulation of ACD6 dependent hyperimmunity by natural alleles of an Arabidopsis thaliana NLR resistance gene. *PLoS Genet* **14**:e1007628.

Zimmermann L, Stephens A, Nam S-Z, Rau D, Kübler J, Lozajic M, Gabler F, Söding J, Lupas AN, Alva V. 2018. A Completely Reimplemented MPI Bioinformatics Toolkit with a New HHpred Server at its Core. *J Mol Biol* **430**:2237–2243.

Figure Supplements

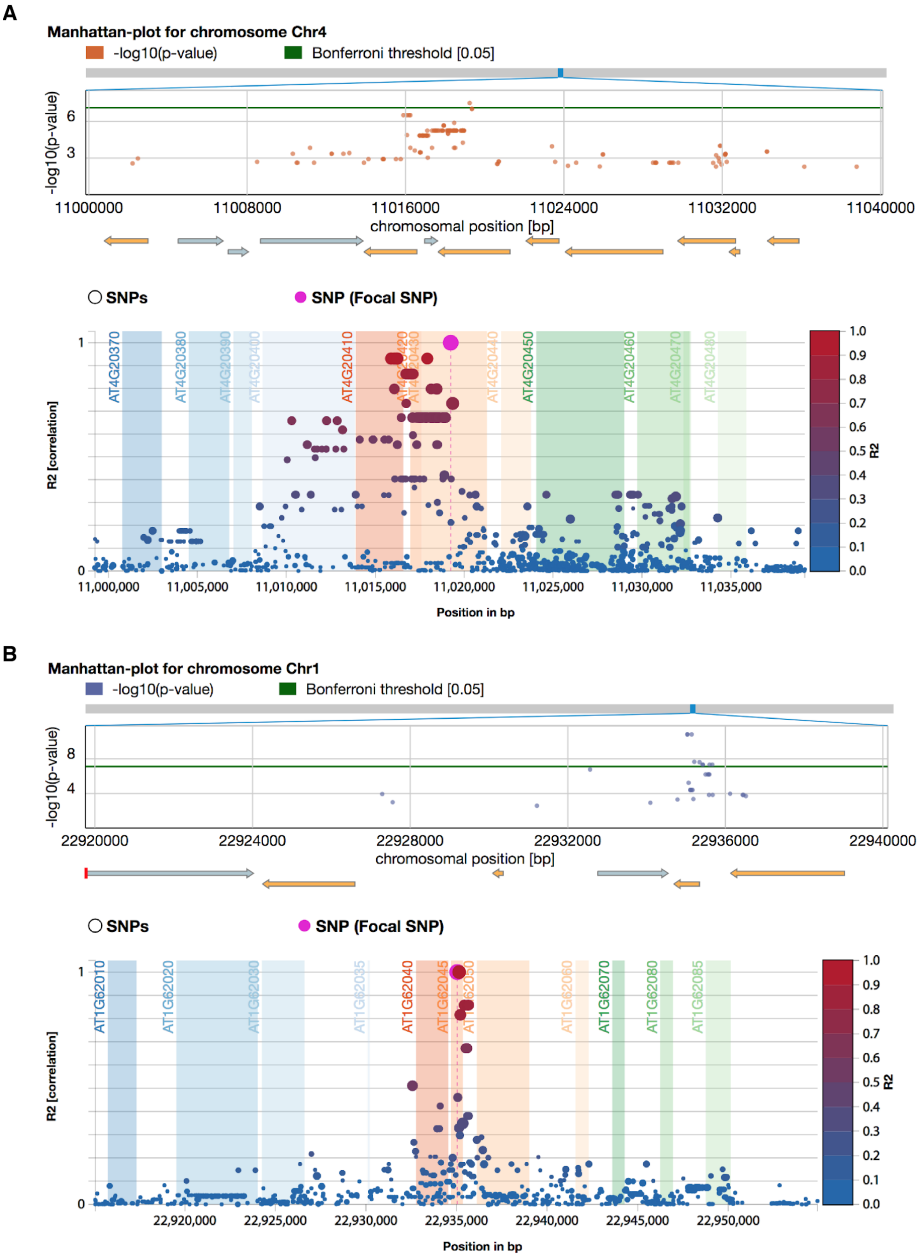

Figure 1–figure supplement 1. GWA of leaf necrosis. (**A**) Top: Genomic region surrounding significant GWA peak for leaf necrosis on chromosome 4 (*MHA2*). Bottom: Linkage disequilibrium (r^2) of SNPs surrounding *MHA2*. (**B**) Top: Genomic region surrounding significant GWA peak for leaf necrosis on chromosome 1 (*MHA1*). Bottom: LD of SNPs surrounding *MHA1*.

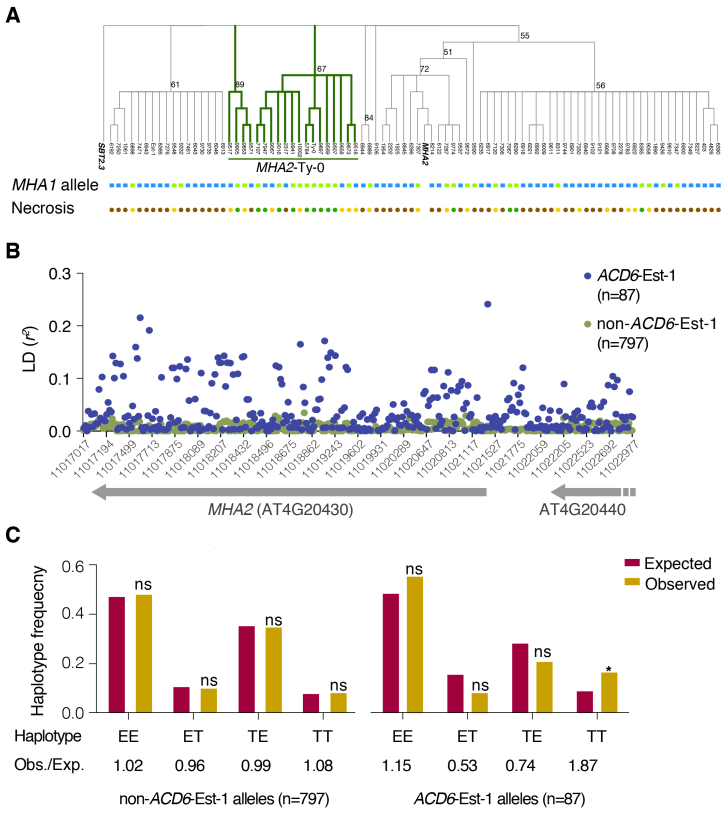

Figure 1–figure supplement 2. Linkage between *ACD6*-Est-1 and different alleles at *MHA1* and *MHA2*. (A) Condensed phylogenetic tree (50% bootstrap cut-off value) using maximum likelihood constructed from phylogeny of *MHA2* DNA sequences from 87 accessions with the *ACD6*-Est-1 allele, together with *MHA2* (*SBT2.2*) and its closest homolog *SBT2.3* from the Col-0 reference genome. Bootstrap values over 50% are indicated at the main branches. Below, *MHA1* allele types in these 87 accessions are presented as light blue (*MHA1*-Est-1) and light green (*MHA1*-Ty-0). Leaf necrosis is indicated as green (weak), orange (intermediate), and brown (severe). The *MHA2*-Ty-0 clade is indicated in dark green. **(B)** Linkage disequilibrium between the causal SNP from *MHA1* (Chr1: 22935037) and SNPs across the *MHA2* locus in 87 *ACD6*-Est-1 and 797 non-*ACD6*-Est-1 accessions. The values of r^2 are statistically significantly different for the two groups (p<0.0001, Wilcoxon nonparametric test). **(C)** Frequency of haplotypes with different *MHA1* and *MHA2* alleles in two populations with *ACD6*-Est-1 and other *ACD6* alleles. The differences between expected and observed haplotype combinations were analyzed by binomial tests for each haplotype; ns, not significant at p>0.05, asterisk: p=0.006 (Bonferroni adjusted). The first letter indicates *MHA1* allele type, the second *MHA2* allele type. E, Est-1 type, T, Ty-0 type.

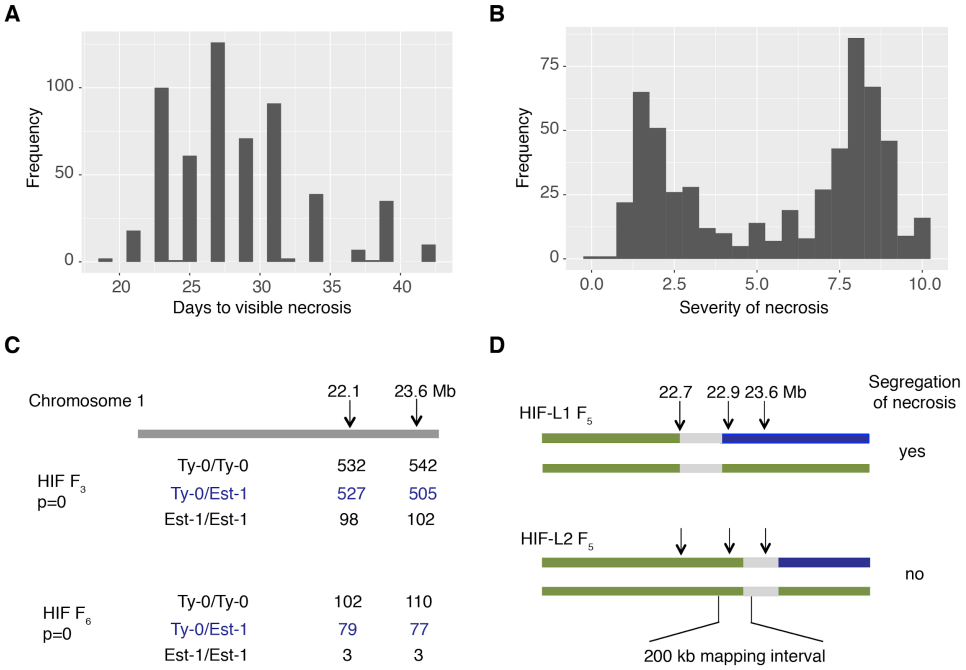

Figure 1–figure supplement 3. QTL analysis and fine-mapping. (**A**) Distribution of days to visible necrosis in 798 F_2 individuals from Est-1 x Ty-0 cross. (**B**) Distribution of subjective severity of necrosis in the same F_2 population as (A). (**C**) Co-segregation of SSLP markers surrounding *MHA1* and absence of leaf necrosis in a Heterogeneous Inbred Family (HIF) in F_3 and F_6 generations. In the F_3 generation, fewer than 10% of individuals without leaf necrosis are fixed for Est-1 alleles at the two markers indicated on top. In the F_6 generation, it is fewer than 2%. *p*-values from χ^2 test indicate differences among genotypic classes (Est-1/Est-1 v. Ty-0/Ty-0 or Ty0/Est-1 at both markers). (**D**) Segregation of leaf necrosis in two HIF lines, differing at *MHA1* locus.

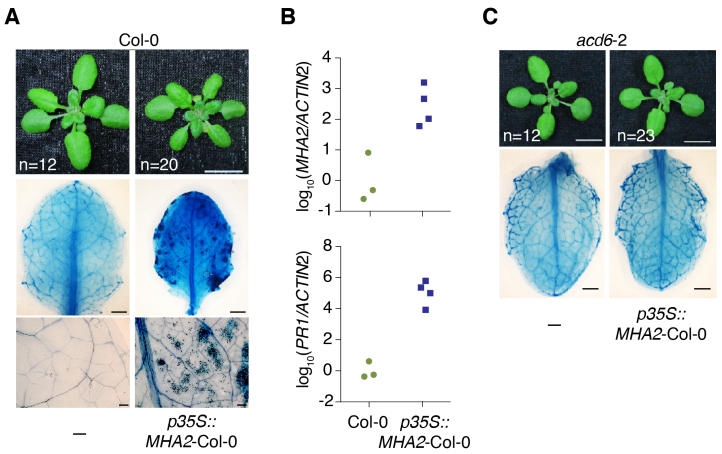

Figure 1–figure supplement 4. Identification of *MHA2* as a genetic modifier of *ACD6*-Est-1. (A) Necrotic leaf phenotype induced by overexpression of *MHA2* (*SBT2.2*) from CaMV 35S promoter. Top, T_1 transformants expressing *p35S::MHA2*-Col-0 in Col-0 background. Representatives of plants without (left) and with (right) the transgene. Middle and bottom, Trypan Blue-stained fifth leaves (entire leaves and close ups). Scale bars, 1 cm (top), 1 mm (middle), 0.1 mm (bottom). **(B)** Accumulation of *MHA2* and *PR1* mRNA, as measured by qRT-PCR from three non-transgenic and four T_1 transgenic plants in Col-0 background. **(C)** Suppression of necrotic leaf phenotype by *acd6-2* loss-of-function allele. Top, T_1 transformants expressing *p35S::MHA2*-Col-0. Representatives of plants without (left) and with (right) the transgene in an *acd6*-2 background. Bottom, Trypan Blue-stained fifth leaves (entire leaves). Scale bars, 1 cm (top), 1 mm (bottom).

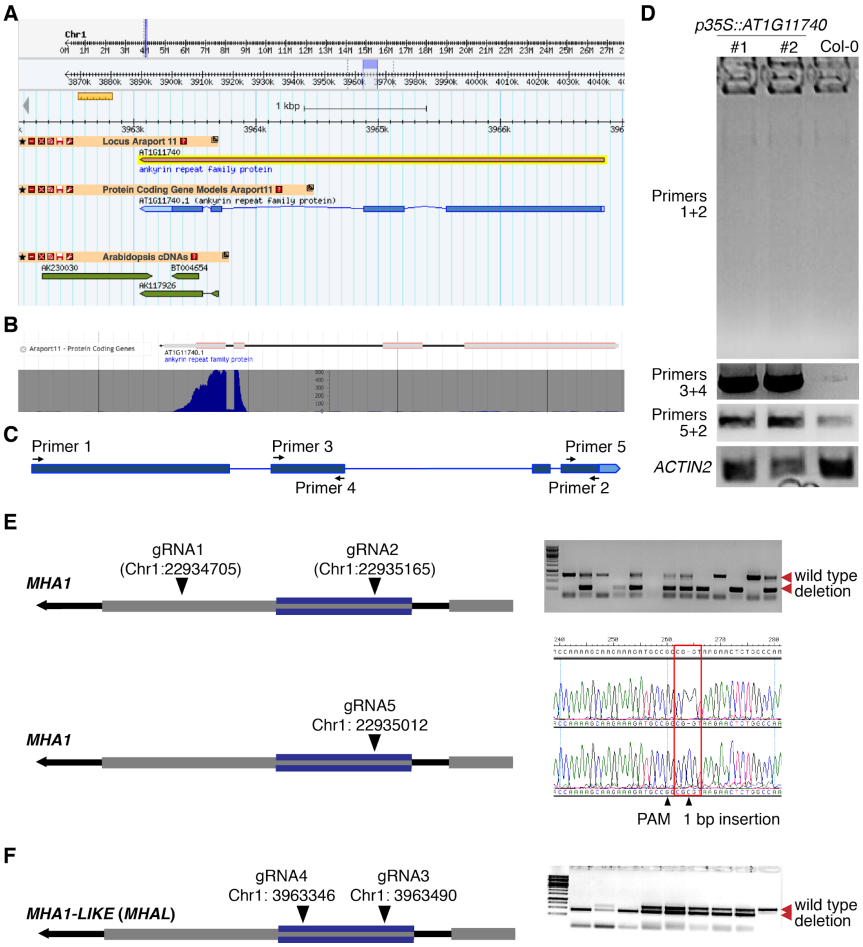

Figure 2–figure supplement 1. *MHA1-LIKE* (*MHAL*) locus and generation of *mha1* and *mhal* mutants. (A) Annotation of AT1G11740 gene model in Araport 11. **(B)** RNA-seq data from light-grown seedlings indicate very different coverages of the 5' and 3' ends of the annotated AT1G11740 gene model. **(C, D)** RT-PCR analysis of Col-0 transformant overexpressing the annotated AT1G11740 gene model. Full-length AT1G11740 cDNA (primers 1+2) cannot be amplified from T_2 transgenic plants or Col-0 plants. A 5' product (primers 3+4) overaccumulates in T_2 transgenic plants, while a 3' product (primers 5+2) accumulates to somewhat higher levels in transgenic compared to Col-0 non-transgenic plants. **(E)** CRISPR-Cas9-induced *mha1* alleles. Left, gRNA positions. Right, genotyping by PCR (top) or Sanger sequencing (bottom). **(F)** CRISPR-Cas9-induced *mhal* alleles in Ty-0. Left, gRNA positions. Right, genotyping by PCR.

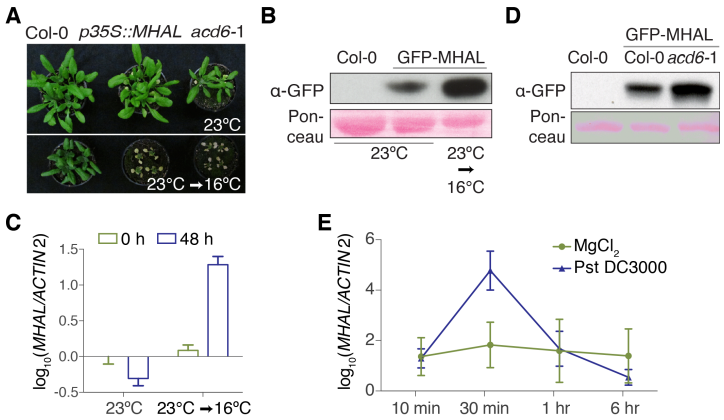

Figure 3–figure supplement 1. *MHAL* acts as a feedforward regulator of *ACD6*. (A) Temperature-dependent phenotypes of *p35S::GFP-MHAL* and *acd6*-1 plants. Top, 3-week-old plants grown in 23°C long days. Bottom, plants grown for 10 days in 23°C long days and then moved to 16°C for 10 days. **(B)** GFP-MHAL protein accumulation in two-week old plants in Col-0 background grown in 23°C long days or plants grown in 23°C long days for 12 days, then moved to 16°C for 2 days. **(C)** Accumulation of *MHAL* mRNA, as measured by qRT-PCR, in non-transgenic two-week old *acd6*-1 plants grown in 23°C long days, or plants grown in 23°C long days for 12 days, then moved to 16°C for 2 days. **(D)** GFP-MHAL protein accumulation in Col-0 and *acd6*-1 backgrounds at 16°C. Plants were from a segregating F_2 population, and 15 individuals each were pooled for protein blot analysis at an early time point. **(E)** Time course of *MHAL* mRNA accumulation, as measured by qRT-PCR, in Col-0 plants after infiltration with *Pseudomonas syringae* pv. *tomato* DC3000 (OD_{600}=0.3).

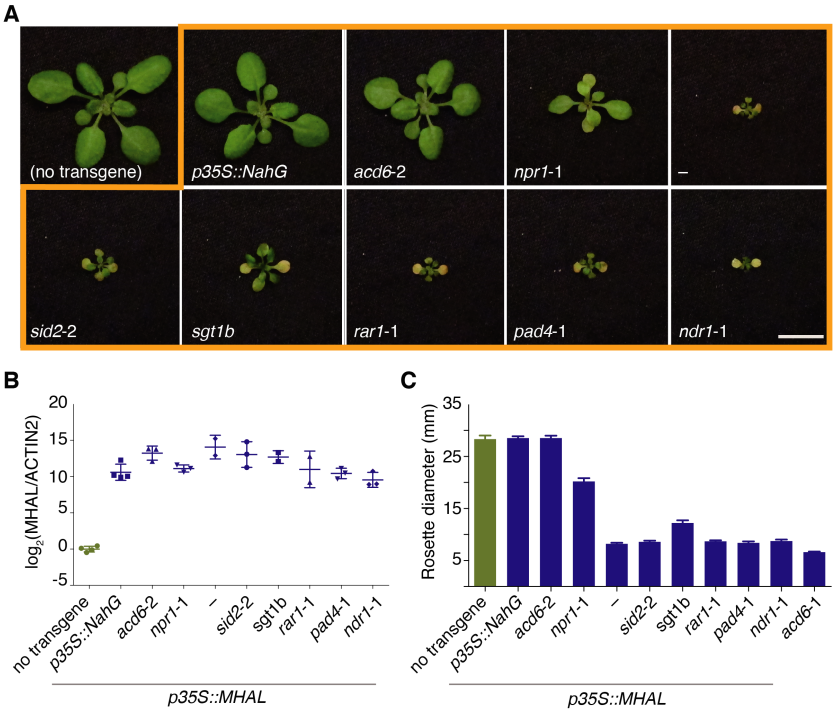

Figure 3–figure supplement 2. Genetic requirement of immune signaling components for *MHAL*-induced necrosis and dwarfism. (A) Representative *p35S::MHAL* T_2 transformants in different backgrounds (thick orange boundary), with non-transgenic Col-0 as control on the top left. Plants were grown at 16°C. **(B)** Accumulation of *MHAL* mRNA in T_2 transformants, as measured by qRT-PCR from three biological replicates each. **(C)** Rosette diameter of T_2 transformants. At least 15 plants were used for each measurement. *acd6-1* for comparison.

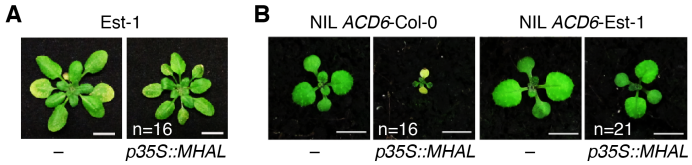

Figure 3–figure supplement 3. *MHAL* activity is *ACD6* allele dependent. 4-week old *p35S::MHAL* T_1 transformants grown under 16°C long day are shown next to non-transgenic controls. (**A**) The effects of *p35S::MHAL* are suppressed in an Est-1 background. Compare to Figure 3B. (**B**) The effects of *p35S::MHAL* are apparent in a NIL (Todesco et al., 2010) with the *ACD6*-Col-0 allele, but not in a NIL with the *ACD6*-Est-1 allele.

A

Hit		Prob	E-value	P-value	Score	SS	Cols	Query HMM	Template	HMM	Organism
3J9P_D	TRPA1	100	3.20E-34	6.80E-39	354.1	41.6	615	5-663	514-1230	-1528	*Homo sapiens*
5VKQ_C	NOMPC	100	9.10E-33	2.00E-37	343.5	45.8	586	46-664	667-1453	-1732	*Drosophila melanogaster*
5WO7_A	TRPV6	99.9	2.40E-28	5.10E-33	278.9	38.2	444	97-664	41-512	-676	*Rattus norvegicus*
6DVW_C	TRPV3	99.9	7.20E-26	1.50E-30	258.4	36.8	415	97-662	115-601	-791	*Mus musculus*
6C8G_A	TRPV4	99.8	2.30E-22	4.90E-27	229.7	28.7	453	90-664	4-502	-675	*Xenopus tropicalis*
6BWJ_B	TRPV2	99.8	3.40E-21	7.20E-26	222.6	33.2	464	97-664	27-557	-776	*Oryctolagus cuniculus*
6BBJ_A	TRPV4	99.8	1.40E-20	3.00E-25	220.8	18.8	294	28-371	10-406	-868	*Xenopus tropicalis*
2PNN_A	TRPV1	99.7	1.50E-18	3.10E-23	173.7	18.8	229	124-428	2-261	-273	*Rattus norvegicus*

B

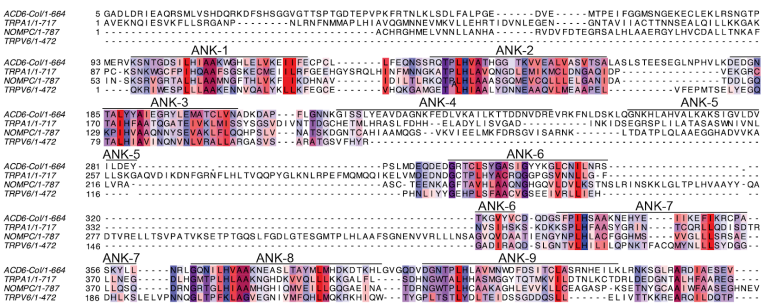

C

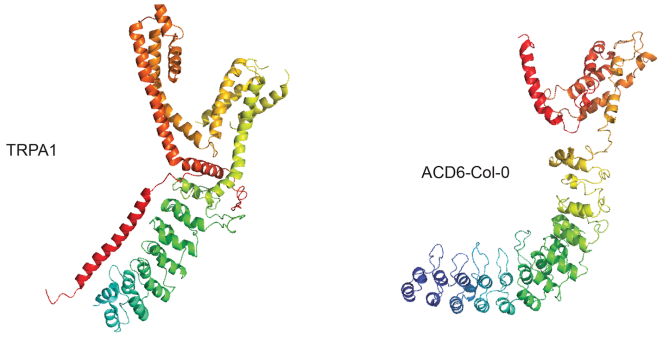

Figure 5–figure supplement 1. Homology modeling of ACD6. (A) HHPred hits with ACD6-Col-0 as query. **(B)** Protein sequence alignment of ankyrin (ANK) repeats of ACD6-Col-0, fly NOMPC, human TRPA1 and rat TRPV6. Coloring indicates hydropathy index. **(C)** Structure of TRPA1 compared to homology modeled ACD6 using Modeller with 2PNN_A, 3J9P_D, 5W07_A, 5VKQ_C, 6DVW_C and 6BBJ_A as templates. Structures are colored from N to C terminus (blue to red). Note that the C-terminal portion of the ACD6 model shows only limited similarity to the TRPA1 pore.

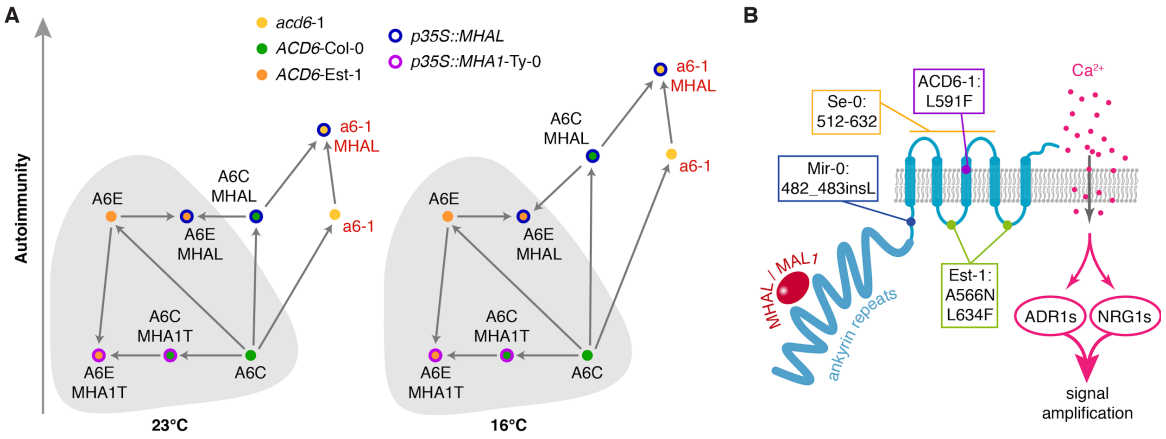

Figure 5–figure supplement 2. Interactions of MHA1, MHAL and ACD6. (A) Summary of genetic interactions between *MHA1*, *MHAL* and *ACD6*. Each arrow denotes a single genetic change. Temperature-insensitive genotypes on top of grey background. The temperature-sensitivity is potentially due to *MHAL* RNA in a wild-type background accumulating to higher levels at 16°C, and also MHAL protein accumulating to higher levels at 16°C, even when expressed from a constitutive promoter. Combinations with the induced allele *acd6*-1 in red. **(B)** Biochemical model for ACD6 function. ACD6 facilitates calcium influx, either by regulating ion channels or acting as an ion channel itself, and its activity is enhanced either by binding of MHAL to its ankyrin repeats, or by mutations in the transmembrane domains. MHA1-Ty-0 can suppress the activity of ACD6-Est-1. Locations of changes in induced and natural gain-of-function alleles are indicated.

Tables

Table 1. Necrosis scores in six individuals each of accessions with *ACD6*-Est-1-like alleles.

Accession ID (1001G)	Name	Country	Latitude	Longitude	Necrosis severity					
403	Zdarec3	CZE	49.3667	16.2667	5	5	5	5	5	5
1061	Brösarp-11-135	SWE	55.7167	14.1333	4	3	4	5	4	4
1890	MNF-Riv-21	USA	43.5139	-86.1859	5	5	5	5	5	5
1925	MNF-Che-2	USA	43.5251	-86.1843	5	5	5	5	5	5
1954	MNF-Jac-12	USA	43.5187	-86.1739	5	5	5	5	5	5
2016	MNF-Pin-39	USA	43.5356	-86.1788	2	2	1	3	2	2
2202	Pent-23	USA	43.7623	-86.3929	5	5	5	5	5	5
2278	SLSP-35	USA	43.665	-86.496	5	5	5	5	5	5
2317	Ste-40	USA	42.03	-86.514	4	4	4	3	5	4
4826	UKSW06-226	UK	50.4	-4.9	5	5	5	5	5	5
5784	Ty-1	UK	56.4	-5.2	2	2	2	3	2	2
6009	Eden-1	SWE	62.877	18.177	5	5	5	5	5	5
6043	Löv-1	SWE	62.801	18.079	5	5	5	5	5	5
6046	Löv-5	SWE	62.801	18.079	5	5	5	5	5	5
6122	T670	SWE	55.8364	13.3075	3	3	2	4	3	3
6192	TDr-5	SWE	55.7692	14.1369	4	4	4	5	3	4
6221	TGR 02	SWE	62.806	18.1896	5	5	5	5	5	5
6235	TOM 01	SWE	62.9611	18.3589	5	5	5	5	5	5
6390	Udul 3-36	CZE	49.2771	16.6314	5	5	5	5	5	5
6396	Udul 4-9	CZE	49.2771	16.6314	5	5	5	5	5	5
6898	An-1	BEL	51.2167	4.4	3	3	3	3	3	3
6900	Bil-5	SWE	63.324	18.484	5	5	5	5	5	5
6901	Bil-7	SWE	63.324	18.484	5	5	5	5	5	5
6908	CIBC-5	UK	51.4083	-0.6383	3	2	4	2	4	3
6913	Eden-2	SWE	62.877	18.177	5	5	5	5	5	5
6917	Fäb-2	SWE	63.0165	18.3174	4	4	4	3	4	5
6918	Fäb-4	SWE	63.0165	18.3174	4	4	4	4	4	4
6922	Gu-0	GER	50.3	8	3	2	3	4	3	3
6940	Mz-0	GER	50.3	8.3	5	5	5	5	5	5
6943	NFA-10	UK	51.4083	-0.6383	4	3	4	4	5	4
6944	NFA-8	UK	51.4083	-0.6383	5	5	5	5	5	4
6945	Nok-3	NED	52.24	4.45	4	3	5	4	3	5

6989	Tamm-2	FIN	60	23.5	3	3	3	2	4	3
6992	Ang-0	BEL	50.3	5.3	5	5	5	5	5	5
7067	Ct-1	ITA	37.3	15	2	1	3	2	2	2
7107	Durh-1	UK	54.7761	-1.5733	2	2	2	2	1	3
7120	En-D	GER	50	8.5	3	2	4	2	4	3
7250	Me-0	GER	51.9183	10.1138	3	3	3	3	3	3
7276	Ob-0	GER	50.2	8.5833	5	5	5	5	5	5
7287	Ove-0	GER	53.3422	8.42255	3	4	2	3	3	3
7306	Pog-0	CAN	49.2655	-123.206	5	5	5	4	5	5
7307	Pn-0	FRA	48.0653	-2.96591	3	2	3	3	4	3
7347	Ste-0	GER	52.6058	11.8558	1	1	2	1	1	1
7349	Ta-0	CZE	49.5	14.5	4	4	4	4	3	5
7350	Tac-0	USA	47.2413	-122.459	3	2	4	3	3	3
7461	H55	CZE	49	15	5	5	5	5	5	5
7471	RLD-1	UNK			5	5	5	5	5	5
7947	PNA3.40	USA	42.0945	-86.3253	2	2	2	2	1	3
8214	Gy-0	FRA	49	2	5	5	5	5	5	5
8227	THÃ– 03	SWE	62.7989	17.9103	5	5	5	5	4	5
8290	En-1	GER	50	8.5	2	2	2	1	2	2
8311	In-0	AUT	47.5	11.5	3	3	3	2	4	3
8366	Sr:5	SWE	58.9	11.2	5	5	5	5	5	5
9058	Västervik	SWE	57.75	16.6333	3	4	2	3	3	3
9067	Xan-3	AZE	38.6536	48.7992	3	4	3	3	2	3
9102	Lag1-4	GEO	41.8296	46.2831	5	5	5	5	5	5
9106	Lag1-8	GEO	41.8296	46.2831	5	5	5	5	5	5
9121	Bak-5	GEO	41.7942	43.4767	3	3	3	2	4	3
9332	Bar 1	SWE	62.8698	18.381	5	5	5	5	5	4
9436	Puk-1	SWE	56.1633	14.6806	4	4	5	4	4	4
9507	IP-Coa-0	POR	38.45	-7.5	1	1	1	1	2	1
9517	IP-All-0	ESP	42.19	-7.8	3	3	2	4	3	3
9518	IP-Alm-0	ESP	39.88	-0.36	1	1	1	1	1	1
9537	IP-Cum-1	ESP	38.07	-6.66	4	3	4	4	4	4
9548	IP-Hoy-0	ESP	40.4	-5	3	2	4	3	3	4
9569	IP-Pds-1	ESP	42.87	-6.45	1	1	1	2	1	1
9571	IP-Pro-0	ESP	43.28	-6.01	4	4	4	4	4	3
9590	IP-Trs-0	ESP	43.37	-5.49	5	5	5	5	5	5

9610	Lesno-4	RUS	53.04	51.96	4	4	4	4	5	3
9611	Lesno-1	RUS	53.04	51.9	3	2	4	3	4	2
9658	Nicas-1	ITA	38.97	16.34	3	3	3	4	2	3
9672	Mitterberg-3-188	ITA	46.37	11.28	3	3	3	3	4	2
9673	Mitterberg-3-189	ITA	46.37	11.28	3	4	2	3	3	3
9708	Kardz-1	BUL	41.62	25.35	5	5	5	5	5	5
9730	Bela-1	SVK	48.47	18.94	5	5	5	5	5	5
9735	Bela-4	SVK	48.47	18.94	5	5	5	5	5	5
9744	Iasi-1	ROU	47.16	27.59	4	4	4	4	5	3
9774	Alt-1	GER	48.59	9.22	1	1	1	1	1	2
9783	Tu-PK-7	GER	48.52	9.05	3	3	3	2	4	3
9853	Lac-0	ESP	43.33	-5.91	3	4	2	3	3	3
9897	Smt-1	ESP	40.95	-5.63	1	1	1	1	2	1
9905	Ven-0	ESP	40.76	-4.01	1	1	1	1	2	1
9941	Fei-0	POR	40.92	-8.54	2	2	2	2	3	1
10002	TueWal-2	GER	48.53	9.04	3	3	3	3	4	3

Table 2. Sequence differences between Ty-0 and Est-1 at *ACD6*. Position relative to Col-0 reference sequence.

SNP	Position	Est-1	Ty-0	Annotation	SNP effect
1	-3393	G	A	Upstream of ATG	Unknown
2	-3375	C	TCC	Upstream of ATG	Unknown
3	-3190	G	T	Upstream of ATG	Unknown
4	-3162	A	deletion	Upstream of ATG	Unknown
5	-3145	C	A	Upstream of ATG	Unknown
6	-3074	C	T	Upstream of ATG	Unknown
7	-2926	T	C	Upstream of ATG	Unknown
8	-2825	A	C	Upstream of ATG	Unknown
9	-2664	C	A	Upstream of ATG	Unknown
10	-2552	A	T	Upstream of ATG	Unknown
11	-2392	G	T	Upstream of ATG	Unknown
12	-2454	A	T	Upstream of ATG	Unknown
13	-2224	A	G	Upstream of ATG	Unknown
14	-2159	G	A	Upstream of ATG	Unknown
15	-1978	C	deletion	Upstream of ATG	Unknown
16	-1977	A	deletion	Upstream of ATG	Unknown
17	-1817	A	C	Upstream of ATG	Unknown
18	-1796	A	C	Upstream of ATG	Unknown
19	-1759	G	A	Upstream of ATG	Unknown
20	-1698	G	deletion	Upstream of ATG	Unknown
21	-1639	T	C	Upstream of ATG	Unknown
22	-1612	T	deletion	Upstream of ATG	Unknown
23	-1611	T	deletion	Upstream of ATG	Unknown
24	-1610	A	deletion	Upstream of ATG	Unknown
25	-1569	C	A	Upstream of ATG	Unknown
26	-1554	T	C	Upstream of ATG	Unknown
27	-1543	A	G	Upstream of ATG	Unknown
28	-1496	A	T	Upstream of ATG	Unknown
29	-1357	G	C	Upstream of ATG	Unknown
30	-1299	A	G	Upstream of ATG	Unknown
31	-1233	G	A	Upstream of ATG	Unknown
32	-1187	T	C	Upstream of ATG	Unknown
33	-1185	G	C	Upstream of ATG	Unknown
34	-1166	T	G	Upstream of ATG	Unknown
35	-1088	T	A	Upstream of ATG	Unknown
36	-1086	A	AT	Upstream of ATG	Unknown
37	-921	T	G	Upstream of ATG	Unknown
38	-755	C	G	Upstream of ATG	Unknown
39	-744	T	deletion	Upstream of ATG	Unknown
40	-698	G	deletion	Upstream of ATG	Unknown
41	-622	A	C	Upstream of ATG	Unknown
42	-572	T	C	Upstream of ATG	Unknown
43	-449	C	A	Upstream of ATG	Unknown
44	990	A	deletion	Intron	Unknown
45	1213	A	T	Intron	Unknown

Table 3. Analysis of EMS induced mutations in 72 *somhal* lines with suppressed *MHAL* overexpression defects. Shown are candidate mutations, which are all G>A (C>T) changes, as typical for EMS, from 52 lines in three genes, *XRN4*, *RST1* and *ACD6*, with multiple hits. Mutations in *RST1* and *XRN4* are known for transgene silencing (Gazzani et al., 2004; Lange et al., 2019; Li et al., 2019). In the remaining 20 lines, mutations were found, but without any overlapping genes. NA, not applicable. Ref., reference base. Alt., alternative base.

Suppressor ID	Gene ID	Gene	Amino acid	Chr.	Pos. (bp)	Ref.	Alt.
269	AT1G54490	*XRN4*	Gln115STOP	1	20,351,481	C	T
57	AT1G54490	*XRN4*	Trp643STOP	1	20,355,270	G	A
225	AT1G54490	*XRN4*	Gln666STOP	1	20,355,433	C	T
242	AT1G54490	*XRN4*	Gln666STOP	1	20,355,433	C	T
243	AT3G27670	*RST1*	Trp119STOP	3	10,245,694	G	A
220	AT3G27670	*RST1*	Trp336STOP	3	10,246,522	G	A
42	AT3G27670	*RST1*	Trp422STOP	3	10,246,874	G	A
110	AT3G27670	*RST1*	Trp422STOP	3	10,246,875	G	A
310	AT3G27670	*RST1*	Trp591STOP	3	10,247,715	G	A
320	AT3G27670	*RST1*	Gln687STOP	3	10,248,260	C	T
8	AT3G27670	*RST1*	Trp705STOP	3	10,248,453	G	A
10	AT3G27670	*RST1*	Trp1158STOP	3	10,250,751	G	A
31	AT3G27670	*RST1*	Trp1360STOP	3	10,251,455	G	A
379	AT3G27670	*RST1*	Gln1800STOP	3	10,253,030	C	T
91	AT3G27670	*RST1*	Gln1803STOP	3	10,253,039	C	T
46	AT4G14400	*ACD6*	Trp111STOP	4	8,296,469	G	A
412	AT4G14400	*ACD6*	Ala186Val	4	8,296,693	C	T
454	AT4G14400	*ACD6*	Ala186Val	4	8,296,693	C	T
363	AT4G14400	*ACD6*	Leu265Phe	4	8,296,929	C	T
528	AT4G14400	*ACD6*	Leu278Phe	4	8,297,096	C	T
194	AT4G14400	*ACD6*	Leu300Phe	4	8,297,162	C	T
78	AT4G14400	*ACD6*	Asp329Asn	4	8,297,249	G	A
191	AT4G14400	*ACD6*	Ala337Val	4	8,297,274	C	T
253	AT4G14400	*ACD6*	Ala338Thr	4	8,297,276	G	A
104	AT4G14400	*ACD6*	Leu368Phe	4	8,297,366	C	T
293	AT4G14400	*ACD6*	Leu368Phe	4	8,297,366	C	T
513	AT4G14400	*ACD6*	Ala371Thr	4	8,297,375	G	A
113	AT4G14400	*ACD6*	Thr402Ile	4	8,297,469	C	T
399	AT4G14400	*ACD6*	His405Tyr	4	8,297,477	C	T
531	AT4G14400	*ACD6*	Ala437Thr	4	8,297,573	G	A

1	AT4G14400	*ACD6*	Ala458Thr	4	8,297,719	G	A
529	AT4G14400	*ACD6*	Ala458Thr	4	8,297,719	G	A
146	AT4G14400	*ACD6*	Thr476Ile	4	8,297,774	C	T
539	AT4G14400	*ACD6*	Ala507Val	4	8,297,867	C	T
406	AT4G14400	*ACD6*	Ala546Thr	4	8,297,983	G	A
95	AT4G14400	*ACD6*	Leu557Phe	4	8,298,016	C	T
70	AT4G14400	*ACD6*	Ala575Thr	4	8,298,070	G	A
122	AT4G14400	*ACD6*	Gly593Asp	4	8,298,125	G	A
337	AT4G14400	*ACD6*	Leu623Phe	4	8,298,214	C	T
449	AT4G14400	*ACD6*	Gly624Asp	4	8,298,218	G	A
540	AT4G14400	*ACD6*	Gly624Asp	4	8,298,218	G	A
274	AT4G14400	*ACD6*	Pro635Leu	4	8,298,251	C	T
34	AT4G14400	*ACD6*	Pro635Leu	4	8,298,251	C	T
413	AT4G14400	*ACD6*	Pro635Leu	4	8,298,251	C	T
472	AT4G14400	*ACD6*	Pro635Leu	4	8,298,251	C	T
308	AT4G14400	*ACD6*	Pro636Ser	4	8,298,253	C	T
200	AT4G14400	*ACD6*	Pro636Leu	4	8,298,254	C	T
421	AT4G14400	*ACD6*	Ser638Phe	4	8,298,260	C	T
435	AT4G14400	*ACD6*	Ser638Phe	4	8,298,260	C	T
475	AT4G14400	*ACD6*	Ser638Phe	4	8,298,260	C	T
489	AT4G14400	*ACD6*	Ser638Phe	4	8,298,260	C	T
391	AT4G14400	*ACD6*	Gly664Asp	4	8,298,338	G	A
4	NA	NA	NA	NA	NA	NA	NA
13	NA	NA	NA	NA	NA	NA	NA
14	NA	NA	NA	NA	NA	NA	NA
21	NA	NA	NA	NA	NA	NA	NA
32	NA	NA	NA	NA	NA	NA	NA
67	NA	NA	NA	NA	NA	NA	NA
82	NA	NA	NA	NA	NA	NA	NA
86	NA	NA	NA	NA	NA	NA	NA
89	NA	NA	NA	NA	NA	NA	NA
183	NA	NA	NA	NA	NA	NA	NA
186	NA	NA	NA	NA	NA	NA	NA
197	NA	NA	NA	NA	NA	NA	NA
245	NA	NA	NA	NA	NA	NA	NA
272	NA	NA	NA	NA	NA	NA	NA
333	NA	NA	NA	NA	NA	NA	NA
344	NA	NA	NA	NA	NA	NA	NA
364	NA	NA	NA	NA	NA	NA	NA

384	NA	NA	NA	NA	NA	NA	NA
425	NA	NA	NA	NA	NA	NA	NA
438	NA	NA	NA	NA	NA	NA	NA

Table 4. Gain-of-function mutations in TRP channel genes.

Channel	Organism	Location	Sequence change	Comments/References
TRP (TRPC1)	Drosophila	S5	F>I	(Hong et al., 2002)
TRPA1	Human	S4	N>S	(Kremeyer et al., 2010)
TRPM3	Human	L4-5 S5	V>M P>Q	(Van Hoeymissen et al., 2020)
TRPM4	Human	ANK ANK-TM linker L3-S4	R>T A>T G>D	(Liu et al., 2010)
TRPM4	Human	S6	I>M I>T A>T	(H. Wang et al., 2019)
TRPC4	Human	C-terminus	I>V	Proposed to affect regulation by Fyn kinase (Jung et al., 2011)
TRPC6	Human	ANK C-terminus	P>Q R>C E>K	(Reiser et al., 2005; Winn et al., 2005)
TRPC6 , TRPML1, TRPML2, TRPML3, TRPV2, TRPV5, TRPV6	Human, mouse	S5 L4-5	A>P C>P V>P RY>P	(Dong et al., 2009; Grimm et al., 2007; Kim et al., 2007; Nagata et al., 2008; Xu et al., 2007)
TRPP2	Human	S5	F>P	(Arif Pavel et al., 2016)
TRPV1	Rat	ANK S5 L5-6	K>E M>T F>L	(Myers et al., 2008a)
TRPV1	Rat	S4 L4-5	R>K G>S	(Boukalova et al., 2010)
TRPV1	Human	L4-5 C-terminus	G>S G>C T>G	(Lin et al., 2012)
TRPV3	Human	ANK-TM linker L4-5 C-terminus	G>S G>C W>G G>A W>C L>F	(Wang and Wang, 2017)
TRPV4, TRPV6	Human	C-terminus	S>D T>D	Mimics phosphorylation by calmodulin (Arbabian et al., 2020)
TRPV4	Human	C-terminus	Frame shift	Proposed to alter regulation by calmodulin (Mah et al., 2016)
TRPV4	Human	ANK	R>C R>H	(Landouré et al., 2010)
TRPY1	Yeast	S5	F>L	(Su et al., 2007)

Table 5. Oligonucleotide primers for SSLP markers.

SSLP marker	Primer sequences	Position (chr 1 bp)	PCR product	
			Ty-0	Est-1
NGA128	GGTCTGTTGATGTCGTAAGTCG		Small	Large
NGA128	ATCTTGAAACCTTTAGGGAGGG	20,633,250		
T13D8	GTTAGCTCTTCCGAGATCTG		Large	Small
T13D8	CGGCGAGAATGATGGAAGGC	22,172,802		
F23C21	ATGGATTAGTTGTGCTACAG		Large	Small
F23C21	TGTTCATGGATATAAATAGA	22,408,632		
T7P1	ATGTACCATCTTACCATTAT		Large	Small
T7P1	GACCATTGGATTGCTAAC	22,422,576		
F11P17	CGCAATCGATTTTATTTAAATCC		Small	Large
F11P17	TTTCAGTTTGATGATTTATTCGC	22,601,704		
T1F9	TTTCAGTTTGATGATTTATTCGC		Small	Large
T1F9	CGCAATCGATTTTATTTAAATCC	22,689,057		
SNP1	GATGTAAATTGGCAGCATATTGATCCT		C	G
SNP1	TATCATTTAGAAGTTCTTTATCCG	22,832,222		
MHA1	AAAACGACGGCGTAATGAAC		Large	Small
MHA1	ATAAGAATCACAATCACTCTTTTTGAG	22,939,031		
SNP2	TGATCTGCACTCTGCGAAAACA		A	G
SNP2	CATCCTCGCTCTCTTCTGTATCGA	23,029,085		
F24D7	TATAACCAGTTTTCAAATCAAC		Small	Large
F24D7	GCTTCTTGTGGTCGTTTT	23,629,412		

Table 6. Guide RNAs for CRISPR/Cas9 genome editing.

sgRNA	sgRNA sequence	Gene	Reference Construct
1	TAATAACATGTAGGCAACT	AT1G62045 (*MHA1*)	pWZ156
2	GGCATCTCCCCGATCCCTC	AT1G62045 (*MHA1*)	pWZ156
3	GGAATTGGGGTGATGGCTG	AT1G11740 (*MHAL*)	pWZ157
4	GATGAAGAATCTTGTGCAG	AT1G11740 (*MHAL*)	pWZ157
5	TGGCCAGAGTTCTTACCGC	AT1G62045 (*MHA1*)	pWZ92

Table 7. Other oligonucleotide primers.

Primer	Sequence	Purpose
G-42937	TAATAACATGTAGGCAACt	Genotyping of *MHA1* CRISPR mutants
G-41414	GGCATCTCCCCGATCCCTC	Genotyping of *MHA1* CRISPR mutants
G-42803	TCATCCAAAATCGGTCATTCTCTCTTTAGT	Genotyping of *MHAL* CRISPR mutants
G-42819	TGGTCAACCAAGAGAATGTGTC	Genotyping of *MHAL* CRISPR mutants
G-17802	TATCCCTAGCTCTTAAGCCGC	Genotyping of *acd6-2*
G-17803	TGGGGTCATCTGGAACTAGTG	Genotyping of *acd6-2*
G-44507	ATGGCAAGTGAAGCACCGAGTTG	qRT-PCR MHA1
G-44508	CTTATCTTTCAAGAATCAGAGTC	qRT-PCR MHA1
G-44610	ATGGCGAGTGAAGCACCTAGTTG	qRT-PCR MAL
G-44644	CTATGAAGAAGTAGAATCCTTC	qRT-PCR MAL
G-16287	ATCACTGCAATTGCCCATGT	qRT-PCR ACD6
G-16288	ACACGCCACACAACCAAAA	qRT-PCR ACD6
G-13182	CGTTCACATAATTCCCACGA	qRT-PCR PR1
G-13183	AAGAGGCAACTGCAGACTCA	qRT-PCR PR1
G-27290	GCCATCCAAGCTGTTCTCTC	qRT-PCR ACTIN2
G-27291	GCTCGTAGTCAACAGCAACAA	qRT-PCR ACTIN2
G-16352	GAGTTTGTAGCCTATTCAAAGGCATT	Cloning, see Table 8
G-40339	CATCGACGTGGCTGAGACTA	Cloning, see Table 8
G-41082	TTATTCGGAACACGCCACACAAC	Cloning, see Table 8
G-41326	GTGTGCCTTCCAATGCTTTT	Cloning, see Table 8
G-41413	GTGTGGTAAACAATTTGTGAG	Cloning, see Table 8
G-41414	GCTAAATCAAAATCGTCTTTC	Cloning, see Table 8
G-41881	GAAAGACGATTTTGATTTAGC	Cloning, see Table 8
G-41882	ATTGCGATATCTTTTCGCAAA	Cloning, see Table 8
G-42331	GATCAGGTACCATGGCAAGTGAAGCACCGA	Cloning, see Table 8
G-42332	TGACTGAATTCTCAAGAATCAGAGTCTTTC	Cloning, see Table 8
G-42591	ACGGGGGACGAGCTCGGTACATGGCAAGTGAAGCACCGA	Cloning, see Table 8
G-42592	GACGCGTACGAGATCTGGTCAGAATCAGAGTCTTTCTTCTTC	Cloning, see Table 8
G-42595	ACGCGTCCCGGGGCGGTACCATGGACAGTTCTGGAGCAGAT	Cloning, see Table 8
G-42596	ACGAACGAAAGCTCTGCAGGTTATTCGGAACACGCCACAC	Cloning, see Table 8
G-42684	CGGGTACCATGGCAAGTGAAGCACCGAG	Cloning, see Table 8
G-42685	AGGTTCGAAAGAATCAGAGTCTTTCTTCT	Cloning, see Table 8
G-42686	CGGGTACCATGGACAGTTCTGGAGCAGATC	Cloning, see Table 8
G-42687	CGATCGATTTCGGAACACGCCACACAAC	Cloning, see Table 8
G-42954	ATGGACAGTTCTGGAGCAGAT	Cloning, see Table 8
G-43182	TACAAACTTTGGATTCACATACA	Cloning, see Table 8
G-43183	AGGTTCGAAGCTTTTGTTTCGTAATTTCAG	Cloning, see Table 8
G-43214	ACGGGGGACGAGCTCGGTACATGGCGAGTGAAGCACCTAG	Cloning, see Table 8

G-43214	ACGGGGGACGAGCTCGGTACATGGCGAGTGAAGCACCTAG	Cloning, see Table 8
G-43241	CGGGATCCATGGACAGTTCTGGAGCAGATC	Cloning, see Table 8
G-43242	AGGGTCGACTCAGCTTTTGTTTCGTAATTTCAG	Cloning, see Table 8
G-43374	AGGTTCGAATGAAGAAGTAGAATCCTTCTTC	Cloning, see Table 8
G-43478	GAGAACACGGGGGACGAGCTCGGTACCTCTACATTCTCCACATTTCCA	Cloning, see Table 8
G-43480	AGTCAGGAACATCGTATGGGTATTCGAATGAAGAAGTAGAATCCTTCTTC	Cloning, see Table 8
G-43790	CGGGTACCATGGCGAGTGAAGCAC	Cloning, see Table 8
G-43791	CGGGATCCTGAAGAAGTAGAATCCTTC	Cloning, see Table 8
G-44140	GAGATTTTTGATGGAATGAGTAAT	Cloning, see Table 8
G-44141	ATTACTCATTCCAtCAAAAATCTC	Cloning, see Table 8
G-44142	CTACATGTGGtTACTCATGGC	Cloning, see Table 8
G-44143	GCCATGAGTAaCCACATGTAG	Cloning, see Table 8
G-44144	ATGGAAATACTGtTCTGTACTACGC	Cloning, see Table 8
G-44145	GCGTAGTACAGAaCAGTATTTCCAT	Cloning, see Table 8
G-44146	TTGCACATGTTGtTTTGAAGGCCAA	Cloning, see Table 8
G-44147	TTGGCCTTCAAAaCAACATGTGCAA	Cloning, see Table 8
G-44148	GGTAGGACTTGTtTTTCATACGGAG	Cloning, see Table 8
G-44149	CTCCGTATGAAAaACAAGTCCTACC	Cloning, see Table 8
G-44150	GTTTTTCATACGaAGCATCCATTGG	Cloning, see Table 8
G-44151	CCAATGGATGCTtCGTATGAAAAAC	Cloning, see Table 8
G-44152	AAGCATCCATTGaGTATTATAAAGG	Cloning, see Table 8
G-44153	CCTTTATAATACtCAATGGATGCTT	Cloning, see Table 8
G-44154	AGTATTATAAAGaACTATGCAACAT	Cloning, see Table 8
G-44155	ATGTTGCATAGTtCTTTATAATACT	Cloning, see Table 8
G-44156	ACGAAATTATTAAAaAGTTTATAAAACGT	Cloning, see Table 8
G-44157	ACGTTTTATAAACTtTTTAATAATTTCGT	Cloning, see Table 8
G-44158	AGGTTCGAACCCGGTGACGTCTTTT	Cloning, see Table 8
G-44159	CGGGTACCATGGCTGCGGAGGAGA	Cloning, see Table 8

G-42275	TGGCCAGAGTTCTTACCGCGTTTTAGAGCTATGCTGAAA	Generation of E-gRNA-MHA1 backbone, related to pWZ092 in Table 8
G-42289	GCGGTAAGAACTCTGGCCACAATCACTACTTCGACTCTA	Generation of E-gRNA-MHA1 backbone, related to pWZ092 in Table 8
G-42795	TAATAACATGTAGGCAACtGTTTTAGAGCTATGCTGAAA	Generation of D-gRNA-MHA1 backbone, related to pWZ156 in Table 8
G-42796	aGTTGCCTACATGTTATTACAATCACTACTTCGACTCTA	Generation of D-gRNA-MHA1 backbone, related to pWZ156 in Table 8
G-42797	GATGAAGAATCTTGTGCAGGTTTTAGAGCTATGCTGAAA	Generation of D-gRNA-MHA1 backbone, related to pWZ156 in Table 8
G-42798	CTGCACAAGATTCTTCATCCAATCACTACTTCGACTCTA	Generation of D-gRNA-MAL backbone, related to pWZ157 in Table 8

G-42560	GGAATTGGGGTGATGGCTGGTTTTAGAGCTATGCTGAAA	Generation of E-gRNA-MAL backbone, related to pWZ157 in Table 8
G-42561	CAGCCATCACCCCAATTCCCAATCACTACTTCGACTCTA	Generation of E-gRNA-MAL backbone, related to pWZ157 in Table 8

Table 8. Key to constructs.

Name	Backbone	Insert	Restriction sites 5'	Restriction sites 3'	Protein tag	Gene
pWZ092	pGreen-IIS	E-ssgRNAs:MHA1	GreenGate		-	AT1G62045
pWZ156	pGreen-IIS	D/E-ssgRNAs:MHA1	GreenGate		-	AT1G62045
pWZ157	pGreen-IIS	D/E-ssgRNAs:MHAL	GreenGate		-	AT1G11736
pWZ019	pFK210	MHA1cDNA (Est-1)	Gateway		-	AT1G62045
pWZ020	pFK210	MHA1 cDNA (Ty-0)	Gateway		-	AT1G62045
pWZ052	pFK210	MHA1 cDNA (Est-1)	Gateway		mGFP	AT1G62045
pWZ053	pFK210	MHA1 cDNA (Ty-0)	Gateway		mGFP	AT1G62045
pWZ054	pFK206	gMHA1 (Est-1)	Gateway		-	AT1G62045
pWZ055	pFK206	gMHA1 (Ty-0)	Gateway		-	AT1G62045
pWZ118	pFK206	gACD6 (Ty-0)	Gateway		-	AT4G14400
pWZ166	pFK206	gACD6 (Est-1)	Gateway		3xFLAG	AT4G14400
pWZ186	pFAST-G02	MHAL CDS	Gibson assembly		-	AT1G11736
pWZ228	pFAST-G02	MHAL CDS	Gibson assembly		mGFP	AT1G11736
pLL134	pUC-19	ACD6 (Col-0)	KpnI	ClaI	3xFLAG	AT4G14400
pLL145	PUC-19	MHA1 (Est-1)	KpnI	Bsp119I	HA-GFP	AT1G62045
pLL175	pUC-19	ACD6-ANK (Col-0)	KpnI	Bsp119I	FLAG	AT4G14400
pLL206	pGEX-6p-1	ACD6-ANK (Col-0)	BamHI	SalI	GST	AT4G14400
pTHE11	pUC-19	MHAL CDS	KpnI	Bsp119I	HA-GFP	AT1G11736
pTHE13	pETM41	MHAL CDS	KpnI	BamHI	MBP-6xHis	AT1G11736
pTHE23	pUC-19	MHAL-N	KpnI	Bsp119I	HA-GFP	AT1G11736
pTHE24	pUC-19	MHAL-C	KpnI	Bsp119I	HA-GFP	AT1G11736
pWZ106	pETM41	MHA1 (Est-1)	KpnI	EcoRI	MBP-6xHis	AT1G62045
pTHE26	pOO2	ACD6 (Col-0)	PstI	SalI	-	AT4G14400
pTHE29	pOO2	MHAL CDS	PstI	SalI	-	AT1G11736
pTHE36	pOO2	ACD6 (ACD6-1)	PstI	SalI	-	AT4G14400
pWZ123	pCAMBIA 1300-nLuc	MHA1 (Est-1)	Gibson assembly		nLUC	AT1G62045
pWZ135	pCAMBIA 1300-nLuc	MHA1 (Ty-0)	Gibson assembly		nLUC	AT1G62045
pWZ122	pCAMBIA 1300-nLuc	ACD6 (Est-1)	Gibson assembly		cLUC	AT4G14400
pWZ144	pCAMBIA 1300-cLuc	ACD6 (Col-0)	Gibson assembly		cLUC	AT4G14400
pWZ182	pCAMBIA 1300-nLuc	MHAL CDS	Gibson assembly		nLUC	AT1G11736